The Astrophysical Journal, 850:74 (31pp), 2017 November 20 https://doi.org/10.3847/1538-4357/aa8ec9

BAT AGN Spectroscopic Survey. I. Spectral Measurements, Derived Quantities, and AGN Demographics

Michael Koss[1,2,16], Benny Trakhtenbrot[2,17], Claudio Ricci[3,4], Isabella Lamperti[1], Kyuseok Oh[1], Simon Berney[1], Kevin Schawinski[1], Mislav Baloković[5], Linda Baronchelli[1], D. Michael Crenshaw[6], Travis Fischer[6], Neil Gehrels[7,18], Fiona Harrison[5], Yasuhiro Hashimoto[8], Drew Hogg[9], Kohei Ichikawa[10], Nicola Masetti[11,12], Richard Mushotzky[9], Lia Sartori[1], Daniel Stern[13], Ezequiel Treister[3], Yoshihiro Ueda[14], Sylvain Veilleux[9], and Lisa Winter[15]
[1] Institute for Astronomy, Department of Physics, ETH Zurich, Wolfgang-Pauli-Strasse 27, CH-8093 Zurich, Switzerland; Mike.koss@eurekasci.com
[2] Eureka Scientific, 2452 Delmer Street Suite 100, Oakland, CA 94602-3017, USA
[3] Instituto de Astrofísica, Facultad de Física, Pontificia Universidad Católica de Chile, Casilla 306, Santiago 22, Chile
[4] Kavli Institute for Astronomy and Astrophysics, Peking University, Beijing 100871, China
[5] Cahill Center for Astronomy and Astrophysics, California Institute of Technology, Pasadena, CA 91125, USA
[6] Department of Physics and Astronomy, Georgia State University, Astronomy Offices, One Park Place South SE, Suite 700, Atlanta, GA 30303, USA
[7] NASA Goddard Space Flight Center, Greenbelt, MD 20771, USA
[8] Department of Earth Sciences, National Taiwan Normal University, No. 88, Section 4, Tingzhou Road, Wenshan District, Taipei 11677, Taiwan Republic of China
[9] Department of Astronomy and Joint Space-Science Institute, University of Maryland, College Park, MD 20742, USA
[10] National Astronomical Observatory of Japan, 2-21-1 Osawa, Mitaka, Tokyo 181-8588, Japan
[11] INAF-Istituto di Astrofisica Spaziale e Fisica Cosmica di Bologna, via Gobetti 101, I-40129 Bologna, Italy
[12] Departamento de Ciencias Físicas, Universidad Andrés Bello, Fernández Concha 700, Las Condes, Santiago, Chile
[13] Jet Propulsion Laboratory, California Institute of Technology, 4800 Oak Grove Drive, MS 169-224, Pasadena, CA 91109, USA
[14] Department of Astronomy, Kyoto University, Kyoto 606-8502, Japan
[15] Atmospheric and Environmental Research, 131 Hartwell Avenue No. 4, Lexington, MA 02421, USA
Received 2016 May 20; revised 2017 July 6; accepted 2017 July 7; published 2017 November 17

Abstract

We present the first catalog and data release of the *Swift*-BAT AGN Spectroscopic Survey. We analyze optical spectra of the majority of the detected AGNs (77%, 642/836)based on their 14–195 keV emission in the 70-month *Swift*-BAT all-sky catalog. This includes redshift determination, absorption and emission-line measurements, and black hole mass and accretion rate estimates for the majority of obscured and unobscured AGNs (74%, 473/642), with 340 measured for the first time. With ∼90% of sources at $z < 0.2$, the survey represents a significant advance in the census of hard X-ray-selected AGNs in the local universe. In this first catalog paper, we describe the spectroscopic observations and data sets, and our initial spectral analysis. The FWHMs of the emission lines show broad agreement with the X-ray obscuration (∼94%), such that Sy 1–1.8 have $N_{\rm H} < 10^{21.9}$ cm^{-2}, and Seyfert 2 have $N_{\rm H} > 10^{21.9}$ cm^{-2}. Seyfert 1.9, however, show a range of column densities. Compared to narrow-line AGNs in the SDSS, the X-ray-selected AGNs have a larger fraction of dusty host galaxies (Hα/H$\beta > 5$), suggesting that these types of AGN are missed in optical surveys. Using the [O III] λ5007/Hβ and [N II] λ6583/Hα emission-line diagnostic, about half of the sources are classified as Seyferts; ∼15% reside in dusty galaxies that lack an Hβ detection, but for which the upper limits on line emission imply either a Seyfert or LINER, ∼15% are in galaxies with weak or no emission lines despite high-quality spectra, and a few percent each are LINERS, composite galaxies, H II regions, or in known beamed AGNs.

Key words: black hole physics – galaxies: active – galaxies: nuclei – quasars: general

Supporting material: machine-readable tables

1. Introduction

A significant population of obscured active galactic nuclei (AGNs) is expected from models and observations of the cosmic X-ray background spectrum (e.g., Comastri et al. 1995; Treister et al. 2009; Draper & Ballantyne 2010; Ueda et al. 2014). The dusty and molecular torus is thought to be responsible for this obscuration and is considered to be a region of 1–100 pc size around the central accreting supermassive black hole (SMBH), with high column densities of $>10^{23}$ cm^{-2}, that absorbs much of the soft X-ray (<10 keV) to optical radiation from the central engine and re-emits it in the infrared (e.g., Pier & Krolik 1992). When the obscuring torus is blocking the line of sight, emission from the broad-line region (BLR) is blocked as well. Even if the line of sight is blocked by the obscuring torus, some direct hard X-ray emission (>10 keV) may still be visible because of the high penetration ability (≈90%, $N_{\rm H} > 5 \approx 10^{23}$ cm^{-2}), provided that the line-of-sight column density is not heavily Compton-thick ($N_{\rm H} > 10^{25}$ cm^{-2}).

Nebular emission lines observed in optical spectra probe the physical state of the ionized gas in galaxies and thus can be used to trace the nuclear activity of, for example, a central SMBH or the instantaneous rate of star formation (Osterbrock & Pogge 1985). Emission-line ratios have been turned into powerful diagnostic tools, not just for individual galaxies, but for massive spectroscopic surveys. Baldwin et al. (1981) first proposed the use of line diagnostic diagrams, which have subsequently been developed and refined in numerous studies (e.g., Veilleux & Osterbrock 1987; Kewley et al. 2001; Shirazi & Brinchmann 2012).

[16] Ambizione fellow.
[17] Zwicky fellow.
[18] Deceased.

While the narrow-line region (NLR) provides a way to detect obscured AGNs in optical surveys, a significant problem is the possible presence of dust in this region. Dust is thought to be destroyed in the BLR, but to extend throughout the NLR (e.g., Mor et al. 2009). This dust will scatter and absorb radiation and substantially change the level of ionization, complicating AGN identification. An additional complication is that in some AGNs, bursts of star formation can overwhelm the AGN photoionization signature (e.g., Moran et al. 2002; Trump et al. 2015). Thus, the largest optical surveys that select AGNs are often incomplete for nearby galaxies because of obscuration or difficulty with detecting lower-luminosity AGNs in galaxies with significant star formation.

An all-sky survey in the ultra-hard X-ray band (14–195 keV) provides an important new way to address several fundamental questions regarding black hole growth and AGN physics, using a complete sample of AGNs. The Burst Alert Telescope (BAT) instrument on board the *Swift* satellite has surveyed the sky to unprecedented depth, increasing the all-sky sensitivity by a factor of ≈20 compared to previous satellites, such as *HEAO 1* (Levine et al. 1984). This has raised the number of known hard X-ray sources by more than a factor of 20 (836 AGNs; Baumgartner et al. 2013). The majority of the BAT AGNs are nearby, with a median redshift of $z \simeq 0.05$ (among the sources with previously known redshifts). This sample is particularly powerful since emission in the 14–195 keV BAT band is relatively undiminished up to obscuring columns of $>10^{24}$ cm^{-2}. BAT is therefore sensitive to heavily obscured objects where even hard X-ray surveys (2–10 keV) are severely reduced in sensitivity. As the brightest AGNs in the sky above 10 keV, BAT-detected AGNs provide an important low-redshift template, as they have similar luminosities to AGNs detected in deep, small-area X-ray surveys that focus on higher redshift AGNs ($z > 1$, see, e.g., Brandt & Alexander 2015, and references therein). Finally, BAT-detected AGNs are also of renewed interest because of a large *NuSTAR* snapshot program, targeting >200 obscured AGNs from *Swift*-BAT (e.g., Baloković et al. 2014; Brightman et al. 2015; Koss et al. 2015, 2016a; Ricci et al. 2016).

Bright AGNs at lower redshifts ($z < 0.2$) offer the best opportunity for high-sensitivity studies of the SMBH accretion rate, which requires accurate measurements of the SMBH mass and AGN bolometric luminosity. Nearby optical spectroscopic studies can provide estimates of the black hole mass through measurements of the velocity dispersions of either the BLR gas and/or the hosts' stars for the majority of AGNs. The emission in the BAT band provides an obscuration-free estimate of the bolometric luminosity. Hence, the combination of optical spectroscopy and hard X-ray emission from the BAT band provides the accretion rate (in terms of the Eddington rate, $L/L_{\rm Edd}$) for a large sample of AGNs. Black hole mass measurements using reverberation mapping (e.g., Bentz et al. 2009), or OH megamasers (e.g., Staveley-Smith et al. 1992) offer more precise measurements of black hole masses; however, these techniques can only be applied to a small ($N < 50$) AGN sample that lacks the uniform selection criteria to understand the AGN population as a whole. Thus, a study of the BAT AGN sample provides an excellent opportunity to study black hole growth in a large sample of uniformly selected nearby AGNs.

Despite the improvement in sensitivity above 10 keV, previous studies of BAT AGNs have been limited to relatively small samples ($N \approx$ 10–100 AGN). The initial 9 month BAT survey, which was based on observations from 2005 to 2006, was studied in two different follow-up programs (e.g., Winter et al. 2010; Ueda et al. 2015). Other BAT optical spectroscopic studies focused on smaller samples (N = 11–75) of newly identified BAT counterparts, such as those from the Palermo BAT catalogs (Parisi et al. 2009, 2012, 2014). Yet other studies focused on small samples of AGNs identified with *INTEGRAL* above 20 keV, with some overlap with the BAT AGNs (e.g., Masetti et al. 2013). While these AGN studies made significant advances in counterpart identification, most did not provide measurements of black hole masses and none measured stellar velocity dispersions in obscured sources.

The goal of this project, the *Swift*-BAT AGN Spectroscopic Survey, or BASS,[19] is to complete the first large ($N \simeq 500$) sample of ultra-hard X-ray-selected AGNs with optical spectroscopy and measured black holes masses using the deep catalogs that detect many more faint AGNs. This enables new insights into the nature and geometry of the obscuring torus and NLR; a measurement of black hole growth in a relatively complete sample of AGNs; and serves as a low-redshift benchmark for deep X-ray surveys of distant AGNs.

In this first paper of a series, we define the AGN sample and provide the results of a set of measurements focusing on emission-line diagnostics, black hole masses, and accretion rates. One of the early science results derived from our analysis—a comparison of X-ray-to-optical line emission—was presented in Berney et al. (2015). In Section 2, we discuss the parent sample of *Swift*-BAT-selected AGNs and the different optical telescopes, instrumental setups, and basic reduction procedures used to collect the spectroscopic data set we use. We describe the host galaxy template fitting, emission-line-fitting, measurements of black hole masses, and bolometric luminosity in Section 3. Finally, the overall AGN spectroscopic properties and initial scientific results and follow-up projects are described in Section 4. Throughout this work, we use a cosmological model with $\Omega_\Lambda = 0.7$, $\Omega_{\rm M} = 0.3$, and $H_0 = 70$ km s^{-1} Mpc^{-1} to determine cosmological distances. However, for the most nearby sources in our sample ($z < 0.01$), we use the mean of the redshift-independent distance in Mpc from the NASA/IPAC Extragalactic Database (NED), whenever available.[20]

2. Parent Sample and Data

In this section we discuss the parent X-ray AGN sample as well as the different databases and dedicated observations used to construct our spectroscopic data set.

2.1. The 70-month Swift -BAT Catalog and X-Ray Data

The BAT survey is an all-sky survey in the ultra-hard X-ray range (>10 keV) that, as of its first 70 months[21] of operation, has identified 1210 objects (Baumgartner et al. 2013). Because of the large positional uncertainty of BAT (≈2′) higher angular resolution X-ray data for every source from *Swift*-XRT or archival data have been obtained, providing associations for 97% of BAT sources. From this catalog, we exclude BAT sources lacking a soft X-ray counterpart, and those associated

[19] The NASA/IPAC Extragalactic Database (NED) is operated by the Jet Propulsion Laboratory, California Institute of Technology, under contract with the National Aeronautics and Space Administration.
[20] www.bass-survey.com
[21] http://heasarc.gsfc.nasa.gov/docs/swift/results/bs70mon/

Table 1
Summary of Instrumental Setups

Telescope	Inst.	Total	Grating	Slit Width (″)	Resolution FWHM [Å]	Total Range [Å]	Velocity Dispersion Fit Range [Å]
SDSS	SDSS	142		2,3	2.76	3900–8000	3900–7000
UK Schmidt	6dF	112	600V, 316R	6.7	5.75	3900–7000	3900–7000
Perkins 1.8 m	Deveny	52	300	2	5.43	3900–7500	3900–5500
KPNO 2.1 m	Goldcam	36	32	2	7.4	4200–8800	4400–5500
		16	26, 35	2	3.3	3900–8500	3900–7000
SAAO 1.9 m	300	46	7	2	5.00	4000–7500	4600–7000
Hale 200 inch	DBSP	20	600	1.5	4.4, 5.8	3900–7000	3900–5500, 8450–8700
		15	600	2	4.8, 6.8	3900–7000	3900–5500, 8450–8700
Gemini 8.1 m	GMOS	21	B600	1	4.84	4000–7000	4000–7000
		5		0.75	3.75	4300–7000	4300–7000
		3		0.75	3.72	4000–7000	4000–7000
CTIO 1.5 m	R–C	10	26, 35	2	4.30	3900–7500	3900–7000
		2	47	2	3.10	5200–7500	5200–7000
		2	36	2	2.20	4500–5500	4500–5500
Tillinghast 1.5 m	FAST	10	300	3	5.5	3700–7500	
UH 2.2 m	SNIFS	5	300	2.4	5.80	3200–7000	3900–5500
APO 3.5 m	DIS	4	B400, R300	1.5	7.00	3900–7000	3900–5600
Shane 3 m	Kast	4	600, 830	2	4.0, 3.2	3900–7000	3900–7000

with galaxy clusters and Galactic sources. In addition, we exclude M82, which is a very nearby star-forming galaxy detected by *Swift*-BAT without the presence of an AGN. This leaves 836 BAT-detected AGNs.

Almost all of the host galaxy AGN counterparts used in this study (99%, 633/642) are based on the published counterparts in the Baumgartner et al. (2013) paper, which was based on *Swift*/XRT, *XMM-Newton*, *Chandra*, *Suzaku*, and *ASCA* follow-up. In Baumgartner et al. (2013), the host galaxy counterpart of the BAT AGN was determined using the brightest counterpart above 3 keV typically from *Swift*/X-Ray Telescope (XRT) observations, within the BAT error radius (≈3′). In only nine cases we use updated galaxy counterparts based on subsequent published studies. These differences are associated with the updated counterparts for SWIFT J1448.7–4009 and SWIFT J1747.7–2253 provided in Masetti et al. (2013); SWIFT J0634.7–7445, SWIFT J0654.6+0700, and SWIFT J2157.4–0615 found in Parisi et al. (2014); SWIFT J0632.8+6343, SWIFT J0632.8+6343, and SWIFT J1238.6+0928 provided in the updated *INTEGRAL* catalog of Malizia et al. (2016), and finally SWIFT J0350.1–5019; we use the counterpart from Ricci et al. (2017) (ESO201-4). Another issue is that some BAT AGN counterparts host dual AGNs (Koss et al. 2016b); however, the median value of the ($L^{\rm int}_{2-10\,{\rm keV}}$) ratio between the dual AGNs is 11 (Koss et al. 2012), so the majority of the emission in the BAT detection is typically coming from a single AGN. A full review of all of the AGN galaxy counterpart identifications and dual AGNs is provided in Ricci et al. (2017).

We then cross-match this sample to the Roma Blazar Catalog (BZCAT) catalog (Massaro et al. 2009) and identify 11% (96/836) of AGNs as possibly beamed sources, such as blazars or flat spectrum radio quasars where Doppler boosting may amplify the non-thermal emission including the hard X-rays. As the Roma BZCAT authors note, classifications of beamed AGNs in their catalog have significant uncertainty because only the very brightest AGNs have the necessary polarimetric observations or detections of compact cores and superluminal motions using high-resolution radio imaging combined with variability studies.

All of the AGNs in the BAT survey have been analyzed using X-ray observations spanning 0.3–195 keV. This includes homogeneous model-fitting using some of the best available soft X-ray data in the 0.3−10 keV band from *XMM-Newton*, *Chandra*, *Suzaku*, or *Swift*/XRT, and the 14–195 keV band from *Swift*/BAT. This analysis provides measurements of the obscuring column ($N_{\rm H}$) and intrinsic X-ray emission ($L^{\rm int}_{2-10{\rm keV}}$). Full details of the X-ray analysis and fitting measurements are provided in separate publications (Ricci et al. 2015, Ricci et al. 2017).

2.2. Optical Spectroscopic Data

The goal of the BASS sample is to use the largest available optical spectroscopic sample of *Swift*-BAT sources using dedicated observations and public archival data. In many cases, there were many duplicate observations of the same source. In such cases, we select the single best spectrum for line measurements for each AGN in our catalog from a single telescope.

For line-fitting, our first criterion was full coverage of the spectral region covering all the lines from Hβ to [S II] λ6717,6731 (i.e., 4800–7000 Å). We then selected, based on the signal-to-noise in the continuum, for fitting of absorption lines and stellar population templates. Each spectrum was visually inspected to avoid any cases that may be problematic for fitting (e.g., bad sky subtraction or noise spikes). This process reduced the number of spectra from 972 spectra including duplicates to 642 unique spectra. Of these 642 unique spectra, 33% (209/642) were from targeted observations and 67% (433/642) were part of archives or previously published papers. A summary of all the observational setups is shown in Table 1 and Figure 1. The original spectra and model fits are available online.[22]

[22] http://www.astro.ethz.ch/bass

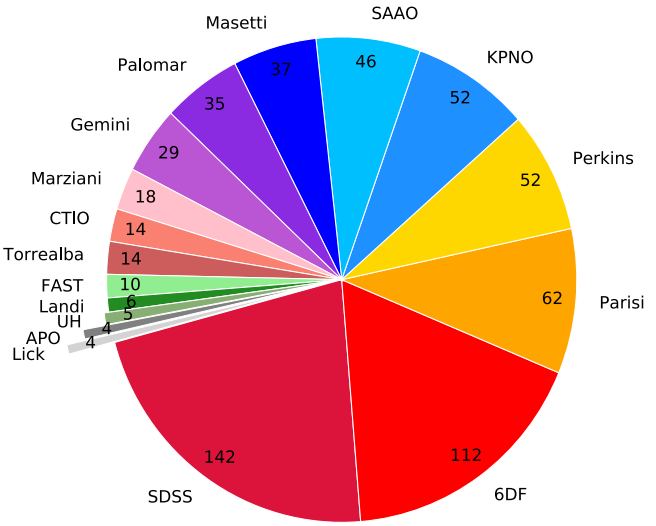

Figure 1. Sources of 642 unique AGN spectra used for the BASS catalog taken from public surveys and targeted campaigns.

2.2.1. Archival Public Data

A large fraction of the data we use are drawn from several large public catalogs of optical spectra. Here, we report on the number of best spectra that were used for each AGN in the catalog. The largest was from the Sloan Digital Sky Survey (York et al. 2000), with 142 sources from data release 12 (DR12, Alam et al. 2015). For 112 additional sources, the spectral measurements are based on archival optical spectra obtained as part of the final data release for the 6dF Galaxy Survey (6dFGS, Jones et al. 2009). The main characteristics of the 6dFGS survey are reported in Jones et al. (2004). We note that, unlike the SDSS spectra, the 6dF spectra are not flux-calibrated on a nightly basis and therefore we have not used them for broad-line black hole mass measurements.

We also used publicly available spectra from smaller compilations of AGNs, as long as they were flux- and wavelength-calibrated and the spectral resolution was well determined. The spectral resolutions were measured based on the FWHM of sky lines in the spectra when possible. For 46 sources, the spectral measurements are based on optical spectra obtained using the SAAO telescope, in an effort to study all of the earlier 9-month survey of BAT AGNs (Ueda et al. 2015). We used 37 spectra from several optical spectroscopic studies of newly identified AGNs from *INTEGRAL* that overlap with the BAT sample in this study (Masetti et al. 2004, 2006a, 2006b, 2006c, 2006d, 2008, 2010, 2012, 2013). For 18 spectra, we used the low-redshift AGN atlas of Marziani et al. (2003), which was obtained using several 2 m class telescopes. Optical spectra of 14 high-redshift AGNs in the BAT sample were obtained through the Monitoring of Jets in AGN with VLBA Experiments (MOJAVE) project, targeting AGNs selected at 2 cm (Torrealba et al. 2012). Ten sources are based on flux-calibrated optical spectra of broad-line AGNs observed with FAST (Landt et al. 2008). We also used spectra obtained to follow-up the Palermo BAT catalog, which has produced its own BAT AGN catalog, which has significant overlap with this sample ($N = 62$; Parisi et al. 2009, 2012, 2014). Finally, we use 6 sources from an early study by Landi et al. (2008) from the first 3-month BAT catalog (Markwardt et al. 2005) that are also detected in the 70-month BAT sample.

2.2.2. Targeted Spectroscopic Observations

The other sources of spectra for our analysis are dedicated spectroscopic observational campaigns of BAT AGN, taken over the last several years using a variety of telescopes and instruments. In terms of the data reduction and analysis, however, we have maintained a uniform approach. All the spectra were processed using the standard tasks in `IRAF` for cosmic ray removal, 1d spectral extraction, and wavelength and flux calibrations. The spectra were all taken as longslit observations, except for observations taken with an Integral Field Unit (IFU) on the University of Hawaii (UH) 2.2 m telescope. In all cases, the listed spectral resolutions were measured based on the FWHMs of sky lines in the spectra or arc lines taken for wavelength calibration. The spectra were flux-calibrated using standard stars, which were typically observed once per night. Basic information about these observations is given in Table 1, and a more detailed account of these dedicated campaigns is presented below.

We had several large, multi-year programs on small 1–2 m telescopes. For 52 sources, the spectral measurements were taken with the KPNO 2.1 m telescope and the GoldCam spectrograph, through a 2″ slit. We used two different setups for observing. The first set of observations was from Winter et al. (2010) and used the grating 26, which covers 3660–6140 Å on the blue side, and the grating 35, which covers 4760–7240 Å on the red side. Both these setups had a spectral resolution of 3.3 Å. Additionally, a separate Goldcam program (PI M. Koss) used a single lower dispersion grating, grating 32, which covered a larger wavelength range than the higher dispersion gratings (4280–9220 Å), at a spectral resolution of 6.7 Å. There were also programs using the Perkins 1.8 m telescope and DeVeny Spectrograph at the Lowell Observatory and CTIO 1.5 m RC spectrograph (PI M. Crenshaw).

We also had optical spectroscopic programs using larger telescopes. For 29 sources, the spectral measurements were obtained with the Gemini North and South telescopes, using the twin Gemini Multi-Object Spectrograph (GMOS) instruments. The GMOS observations took place between 2009 and 2012, as part of nine different observing programs (P.I. M. Koss, E. Treister, and K. Schawinski). In this study we use data from Gemini programs GN-2009B-Q-114, GN-2010A-Q-35, GN-2011A-Q-81, GN-2011B-Q-96, GN-2012A-Q-28, GN-2012B-Q-25, GS-2010A-Q-54, and GS-2011B-Q80. Most of these programs focused on dual AGNs, but covered the brighter BAT sources with the slit aligned with the secondary galaxy nucleus. We used two spectral setups for observations. The majority of targets were observed using the B600-G5307 grating with a 1″ slit in the 4300–7300 Å wavelength range, providing a spectral resolution of 4.8 Å. The Gemini/GMOS `IRAF` pipeline was used for wavelength calibration, spectro-spatial flat-fielding, cosmic ray removal, and flux calibration.

We used the Palomar Double Spectrograph (DBSP) on the Hale 200 inch Hale telescope for 35 targets. These AGNs were observed as part of the *NuSTAR* BAT snapshot program, focusing mostly on Seyfert 2 AGNs (P.I. F. Harrison and D. Stern). The observations were performed between 2012 October and 2015 February. The majority of observations were taken with the D55 dichroic and the 600/4000 and 316/7500 gratings using a 1.″5 slit, providing resolutions of 4.4 Å and 5.8 Å, respectively.

Finally, we had smaller programs using the 3.5 m Apache Point telescope (APO, 4 sources), the 3 m Shane telescope at the Lick observatory (4 sources), and the UH 2.2 m telescope (5 sources). The APO observations used the B400 and R300 gratings with a 1.″5 slit, providing wavelength coverage from 3570 to 6230 Å in the blue and 5190–9810 Å in the red and resolution of 7 Å. The Lick observatory Kast spectrograph was used with blue and red coverage between 3900 and 7000 Å and a spectral resolution of 4 Å. On the UH telescope, we used the SuperNova Integral Field Spectrograph (SNIFS). SNIFS has a blue (3000–5200 Å) and red (5200–9500 Å) channel, with a resolution of 5.8 Å in the blue and 8.0 Å in the red. The SNIFS reduction pipeline, `SNURP`, was used for wavelength calibration, spectro-spatial flat-fielding, cosmic ray removal, and flux calibration (Bacon et al. 2001; Aldering et al. 2006). A sky image was taken after each source image and subtracted from each IFU observation. The extraction aperture was 2.″4 in diameter.

3. Spectroscopic Measurements

We performed three separate sets of spectral measurements with the 642 BASS spectra. The general properties of each AGN and the details of the optical spectra are presented in Table 2. In the first step, each AGN host galaxy was fit using galaxy stellar templates (Section 3.1) and the velocity dispersion was measured when possible (Section 3.1.1). The emission lines were then fit (Section 3.2) using narrow components and broad components when needed. Black hole masses in AGNs with broad emission lines were measured by a more detailed fit to the spectral regions that included the broad Hβ and/or broad Hα lines, or the Mg II λ2798 and C IV λ1549 lines in high-redshift sources (Section 3.3). Finally, we estimated the bolometric luminosity ($L_{\rm bol}$) from the X-ray luminosity to estimate the accretion rates (Section 3.4).

3.1. Galaxy Template Fitting

We use the penalized PiXel Fitting software (`pPXF`; Cappellari & Emsellem 2004) to measure stellar kinematics and the central stellar velocity dispersion (σ_*). This method operates in pixel space and uses a maximum penalized likelihood approach for deriving the line-of-sight velocity distribution (LOSVD) from kinematic data (Merritt 1997). As a first step, the PPXF code (version 5.1.9) creates a model galaxy spectrum $G_{\rm mod}(x)$ by convolving empirical stellar population models by a parameterized LOSVD. Then, it determines the best-fitting parameters of the LOSVD by minimizing the value of χ^2, which measures the agreement between the model and the observed galaxy spectrum over the set of reliable data pixels used in the fitting process. Finally, PPXF uses the "best-fit spectra" to calculate the velocity dispersion and associated uncertainty from the absorption lines.

The PPXF code uses a large set of single stellar populations to fit each galaxy spectrum. We used the templates from the Miles Indo-U.S. Catalog (MIUSCAT) library of stellar spectra (Vazdekis et al. 2012). The MIUSCAT library of stellar spectra contains ≈1200 well-calibrated stars covering the spectral region of 3525–9469 Å at a spectral resolution of 2.51 Å (FWHM). These spectra are then computed into stellar libraries with an IMF slope of 1.3, and the full range of metallicities ($M/H = -2.27$ to $+0.40$) and ages (0.03–14 Gyr). These templates have been observed at higher spectral resolution (FWHM = 2.51 Å) than the AGN observations and are convolved in PPXF to the spectral resolution of each observation before fitting.

We fitted the spectra in the wavelength region 3900–7000 Å, if this entire range was covered by the given spectrum. This range covers the Ca H+K λ3935, 3968 and Mg I λ5175 absorption features. For some spectra the velocity dispersion was estimated only based on the Mg I absorption line, because of a lack of blue wavelength coverage (e.g., spectra taken with KPNO and grating 32, Perkins, and some Gemini gratings). To avoid complications with discontinuities and dispersion changes in spectra that have both blue and red setups, only the blue channel spectra (3800–5500 Å) were used to estimate velocity dispersion, focusing on the Ca H+K and Mg I absorption lines. The only exception is the dual-channel SDSS data, where the full range was fit. Whenever available, we also fitted the Ca II triplet spectral region (8450–8700 Å).

We modified the `ppxf-kinematics-example-sdss` code to measure stellar kinematics in our sample. Table 3 shows the emission and bright night sky lines that were masked. The code automatically applies a mask for several bright emission lines: Hδ, Hγ, Hβ, [O III] λ5007, [O I] λ6300, [N II] λ6583, Hα, and [S II] λ6717,6731. We masked sky lines at λ5577, λ6300, λ6363, and λ6863. We also mask the region around the Ca H λ3968 line, because of overlap with the Hϵ λ3970 and the [Ne III] λ3968 emission lines (see, e.g., Greene & Ho 2005a). We have also masked the region surrounding the Na I line, since it may be affected by interstellar absorption. Finally, we masked regions affected by sky emission lines. The width of these emission-line masks was set to 2400 km s^{-1}. For the broad-line AGNs, we use a wider mask (3200 km s^{-1}) for the Balmer lines (Hα, Hβ, Hγ, Hδ), in order to mask the broad emission components. This allowed us to measure the velocity dispersion for some AGNs with broad emission in Hα, but narrow Hβ.

3.1.1. Velocity Dispersion Measurements

Figure 2 summarizes the results of the stellar velocity dispersion measurements and individual measurements are found in Table 4. $\Delta\sigma_*$ denotes the error in σ_*. We were able to achieve a reliable velocity dispersion measurement, with $\Delta\sigma_* < 60$ km s^{-1}, in 201 of the 642 (31.3%) galaxies in our sample. For these AGNs, the stellar continuum was subtracted prior to emission-line-fitting (discussed below). For most AGNs with broad Hβ, the AGN continuum contaminated the host galaxy and stellar absorption lines, limiting reliable σ_* measurements to only 13 type 1.2–1.8 AGNs. Additionally, in 166 sources the signal-to-noise ratio and spectral resolution were too low to robustly identify the absorption lines.

Four authors (M.K., B.T., S.B., and I.L.) visually inspected the fit of the stellar continuum and absorption lines, and assigned a quality flag to each spectrum. In our sample we have 128 spectra with flag 1 and 73 spectra with flag 2, which both designate reliable measurements. More details and examples of these quality flags are given in the Appendix A.1. Generally, the σ_* uncertainty measured by PPXF for flag 1 fits is typically small ($\langle\Delta\sigma_*\rangle \simeq 12$ km s^{-1}). Flag 2 fits have somewhat worse quality fits, judged from our visual inspection, consistent with PPXF measurements ($\langle\Delta\sigma_*\rangle \simeq 27$ km s^{-1}), but the Ca H+K and Mg I absorption lines are still well fit.

For AGNs with reliable measurements of σ_* we calculated the black hole mass, $M_{\rm BH}$, using the $M_{\rm BH}$–σ_* relation. We use

Table 2
Optical spectra

ID[a]	Counterpart Name	Source	$z_{[O\ III]}$[b]	Distance (Mpc)	log L_{14-195}[c] (erg s^{-1})	log L_{bol}[d] (erg s^{-1})	Date yyyy/mm/dd	Exp. (s)	Slit Width (kpc)	Type[e]	Beamed[f]	N_H[g]
1	2MASX J00004876−0709117	SDSS	0.037	165.14	43.63	44.53	2013 Oct 25	5401	1.54	1.9	0	Obs.
2	Fairall 1203	6DF	0.058	261.64	43.92	44.82	2005 Sep 01	1200	8.02	1.9	0	$<10^{20}$ cm^{-2}
4	2MASX J00032742+2739173	SDSS	0.040	175.13	43.68	44.58	2013 Sep 09	4500	1.63	2.0	0	Obs.
5	2MASX J00040192+7019185	Masetti	0.096	442.73	44.47	45.38	2006 Nov 27	1800	⋯	1.9	0	Obs.
6	Mrk 335	Perkins	0.026	113.28	43.45	44.36	2011 Apr 01	1800	1.07	1.2	0	Unobs.
7	2MASX J00091156−0036551	SDSS	0.073	331.27	44.09	44.99	2000 Sep 06	2700	4.49	2.0	0	Obs.
8	Mrk 1501	Gemini	0.089	408.45	44.80	45.70	2012 Aug 17	595	1.82	1.5	1	Unobs.
10	2MASX J00210753−1910056	6DF	0.096	439.38	44.60	45.50	2003 Aug 27	1200	13.01	1.9	0	Unobs.
13	2MASX J00253292+6821442	Palomar	0.012	53.99	42.80	43.71	2014 Dec 23	150	0.50	2.0	0	Obs.
14	2MASX J00264073–5309479	6DF	0.063	283.63	44.13	45.04	2005 Jul 03	1200	8.62	1.9	0	$<10^{20}$ cm^{-2}

Notes.
[a] *Swift*-BAT 70 month hard X-ray survey ID (http://swift.gsfc.nasa.gov/results/bs70mon/).
[b] Redshift measured from [O III] λ5007.
[c] *Swift*-BAT X-ray luminosity (14–195 keV).
[d] Bolometric luminosity estimated from the *Swift*-BAT X-ray luminosity (14–195 keV).
[e] AGN classification following Osterbrock (1981).
[f] Flag presenting beamed AGNs ("1").
[g] Obscuration flag distinguished by hydrogen column density: "Obs." for $N_H > 10^{22}$ cm^{-2} and "Unobs." for $N_H < 10^{22}$ cm^{-2}. Further details on the column density can be found in Ricci et al. (2017).

(This table is available in its entirety in machine-readable form.)

Table 3
Emission Lines Masked in pPXF Host Galaxy Fitting

Emission Line	Wavelength [Å]
[O II]	3726.03
	3728.82
CaH	3968.47
Hδ	4101.76
Hγ	4340.47
He II	4686.00
Hβ	4861.33
[O III]	4958.92
	5006.84
[N I]	5200.00
[Fe VII]	5721.00
NaD	5890.00
NaD	5896.00
[O I]	6300.3
[N II]	6548.03
	6583.41
Hα	6562.8
[S II]	6716.47
	6730.85
Sky	5577.00
Sky	6300.00
Sky	6363.00
Sky	6863.00

the relation from Kormendy & Ho (2013):

$$\log\left(\frac{M_{\rm BH}}{M_{\odot}}\right) = 4.38 \times \log\left(\frac{\sigma_{*}}{200\ {\rm km\ s^{-1}}}\right) + 8.49. \quad (1)$$

The slope of this relation is shallower than the slope of the relation from McConnell & Ma (2013), who reported a value of 5.64, and is consistent with the slope of the relation from Gültekin et al. (2009). A small number of sources have direct measurements of black hole masses, either from reverberation mapping (39) or OH megamasers (8), which we have adopted and tabulated whenever available.

3.2. Emission-line Measurements

We fit emission lines in our sample of optical spectra using an extensive spectroscopic analysis toolkit for astronomy, `PySpecKit`, which uses a Levenberg–Marquardt algorithm for spectral fitting (Ginsburg & Mirocha 2011). All emission-line fits were visually examined by five authors (M.K., B.T., S.B., K.S., and I.L.) to verify proper fitting, and to adjust some subtle parameters. We implement separate methods for fitting sources with only narrow lines and for sources with broad lines. For narrow-line sources, we first fit and subtract a host stellar component, to remove the galaxy continuum and stellar absorption features, as described in Section 3.1. We then separately fit three spectral regions, focusing on the [O II] (3300–4000 Å), Hβ (4650–5050 Å), and Hα (6250–6770 Å) emission lines. All measurements for narrow-line sources are listed in Tables 5–7 for the [O II] λ3727, Hβ, and Hα regions measurements, respectively. The emission-line classifications are provided in Table 8. For broad-line sources, the properties are listed in Table 9 for both Hβ and Hα.

For 6DF spectra, the survey applied a single calibration to all spectra to convert measured counts to the correct spectral shape, but a nightly flux calibration was not applied. For 6DF emission-line measurements, we have calculated a rough flux calibration factor for 6DF spectra based on 12 overlapping spectra in distant AGNs ($z > 0.05$) with the SDSS. This factor assumes 1 ct is equal to 7.69×10^{-17} erg s^{-1} cm^{-2} AA^{-1}.

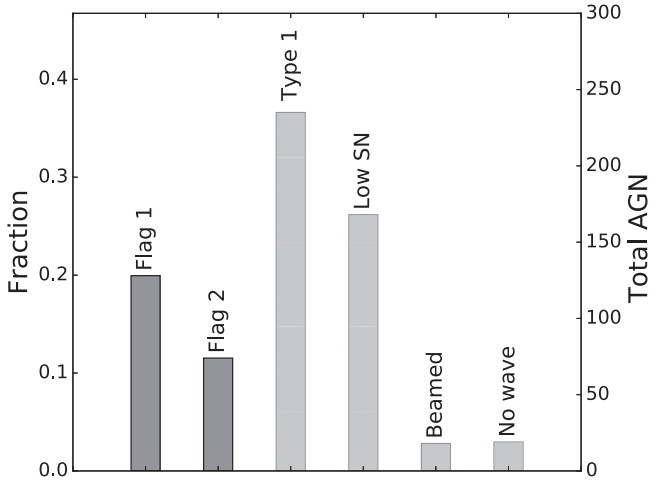

Figure 2. Measurements of velocity dispersion from our sample using pPXF. For 31% of spectra (201/642), we have a robust measurement of σ_{*}. 128 spectra have a good fit and small error in the value of σ_{*} (flag 1). 73 spectra have worse fits, but the value of σ_{*} is sufficiently good based on visual inspection (flag 2). The remaining categories (dashed histograms) have features that prevented measurements. For 207 spectra we could not measure σ_{*} because of AGN contamination to the stellar continuum. For 166 spectra, the signal-to-noise levels of the continuum or the grating resolution were not sufficient to measure the absorption lines. A small number of sources were blazars with featureless continua. Finally, we also had a small number of sources with no coverage of key absorption line features such as Ca H+K, Mg I, or the Ca II triplet regions.

In each of the three spectral fitting regions, we adopt a power-law fit (1st order) to account for the (local) AGN continuum and a series of Gaussian components to model the emission lines. We define an emission-line detection when we reach a S/N > 3 over the line with respect to the noise of the adjacent continuum, and otherwise list upper detection limits. To estimate errors in line fluxes and widths (in terms of FWHM), we use a simple re-sampling procedure that adds noise based on the error spectrum and reruns the fitting procedure 10 times. The (fractional) flux uncertainty for the [O III] emission line is typically less than 1%. We use the narrow Balmer line ratio (Hα/Hβ) to correct for dust extinction, assuming an intrinsic ratio of $R_{\rm V} = 3.1$ and the Cardelli et al. (1989) reddening curve. In the case of a Hβ non-detection, we assume the 3σ upper limits for the extinction correction. When neither Hβ nor Hα are detected we present the fluxes as measured.

For the Hβ spectral region, we fit the He II λ4686, Hβ, [O III] λ4959, and [O III] λ5007 lines. The widths of the narrow lines are tied with an allowed variation of $\pm$500 km s^{-1}. The central wavelength of the NLR is defined by a joint fit of all the narrow lines where the wavelength separation of all lines is tied. The intensity of [O III] λ4959 relative to [O III] λ5007 is fixed at the theoretical value of 2.98 (Storey & Zeippen 2000) and the intensity of [N II] λ6548 relative to [N II] λ6583 is set to the theoretical value of 2.96 (Acker et al. 1989). For the Hβ complex, we use the 4660–4750 Å (except around He II) and 5040–5200 Å regions for continuum determination. Within the Hα spectral region, we fit the [O I] λ6300, [N II] λ6548, Hα, [N II] λ6583, and [S II] λ6716, and [S II] λ6731 lines. Here too, the widths of the narrow lines are tied, with an allowed variation of $\pm$500 km s^{-1}, and the systemic redshift is

Table 4
Stellar Velocity Dispersion Measurements

ID[a]	Source	Redshift[b]	σ (km s^{-1})	log $M_{BH}/M_{\odot}$	Flag$_{\sigma}$[c]	Ca H+K[d]	Mgb[e]	σ_{CaT}[f] (km s^{-1})	CaT[g]	$\sigma_{lit.}$ (km s^{-1})	log$(M_{BH}/M_{\odot})_{lit.}$[h]	References[i]
1	SDSS	0.03767	152 ± 6	7.97 ± 0.30	1	1	1	...	...	...	...	...
2	6DF	0.05846	180 ± 38	...	7	1	1	...	...	...	...	...
4	SDSS	0.03970	142 ± 7	7.85 ± 0.30	1	1	1	...	...	...	...	...
5	Masetti	...	...	...	9	1	1	...	...	...	...	...
6	Perkins	...	...	...	9	1	1	...	...	...	...	...
7	SDSS	0.07334	250 ± 16	8.91 ± 0.32	1	1	1	...	...	...	...	...
8	Gemini	...	...	...	9	0	1	...	...	...	...	...
10	6DF	0.09561	284 ± 21	9.16 ± 0.32	2	1	1	...	...	...	...	...
13	Palomar	...	...	...	9	1	1	...	9	...	...	...
14	6DF	0.06286	326 ± 49	...	7	1	1	...	...	...	...	...

Notes.
[a] *Swift*-BAT 70-month hard X-ray survey ID (http://swift.gsfc.nasa.gov/results/bs70mon/).
[b] Redshift measured from the stellar template.
[c] Quality flag: 1—excellent fit with small error ($\langle\sigma_*\rangle$ error = 11 km s^{-1}, $\sigma_* < 34$ km s^{-1}), 2—larger errors than flag 1 ($\langle\sigma_*\rangle$ error = 23 km s^{-1}, $\sigma_* < 60$ km s^{-1}), but acceptable fit, 3—bad fit with high S/N, 7—presence of broad component at Hβ or Hα, 8—very weak absorption features, 9—bad fit.
[d] Flag = 1 when Ca H+K λ3935, 3968 is fitted.
[e] Flag = 1 when Mg I is fitted.
[f] σ_* measured from Ca II triplet.
[g] Flag = 1 when Ca II triplet is fitted.
[h] Black hole mass from literature: C05 (Capetti et al. 2005); C09 (Cappellari et al. 2009); D03 (Devereux et al. 2003); H05 (Herrnstein et al. 2005); K08 (Kondratko et al. 2008); K11 (Kuo et al. 2011); L03 (Lodato & Bertin 2003); M11 (Medling et al. 2011); O14 (Onken et al. 2014); RJ06 (Rothberg & Joseph 2006); T03 (Tadhunter et al. 2003); TYK05 (Trotter et al. 1998; Yamauchi et al. 2004; Kondratko et al. 2005); W06 (Wold et al. 2006); W12 (Walsh et al. 2012).
[i] Reference for $\sigma_{lit.}$: C04 (Cid Fernandes et al. 2004); F00 (Ferrarese & Merritt 2000); G05 (Garcia-Rissmann et al. 2005); G13 (Grier et al. 2013); Hy (http://leda.univ-lyon1.fr); H09 (Ho et al. 2009); L17 (Lamperti et al. 2017); M13 (McConnell & Ma 2013); NW95 (Nelson & Whittle 1995); N04 (Nelson et al. 2004); RJ06 (Rothberg & Joseph 2006); V15 (van den Bosch et al. 2015).

(This table is available in its entirety in machine-readable form.)

determined from all narrow lines. In the case of a non-detection of the narrow Hα or [S II] λ6717,6731 line (i.e., due to a very strong broad Hα component or weak narrow emission lines), we use the FWHM of [O III] λ5007 to constrain the widths of the narrow lines in the Hα region. The relative strengths of [N II] λ6548 and [N II] λ6583 lines are fixed at 1:2.94. To estimate the continuum for the Hα complex, we use the wavelength regions 5800–6250 Å and 6750–7000 Å. Finally, within the [O II] spectral region, we fit the [Ne V] λ3346, [Ne V] λ3426, [O II] λ3727, [Ne III] λ3869, and [Ne III] λ3968 lines. The continuum around the [O II] spectral region is usually more complicated to fit due to a nonlinear shape or because it lies near the blue edge of the wavelength coverage. To fit this blue continuum, we use the region between 3300 and 4000 Å, except for small regions surrounding the emission lines themselves ($\pm$1000 km s^{-1}).

For sources with broad Hβ, we use the fitting procedure described in detail in Trakhtenbrot & Netzer (2012; see Appendix C1 therein), and here we provide only a brief description of the key spectral components. The AGN spectrum is first fitted with a linear (pseudo-) continuum, based on two narrow ($\pm$10 Å) continuum bands, typically around 4440 Å (or 4720 Å) and 5110 Å. Next, a broadened and shifted iron emission template (Boroson & Green 1992) is fitted to and subtracted from the continuum-free spectrum. Then, we fit the remaining emission lines with a set of Gaussian profiles. In particular, the narrow components of Hβ, [O III] λ4959, and [O III] λ5007 are fitted with a single Gaussian profile, while the broad components of He II and Hβ are described by two Gaussian components (each). As described in Trakhtenbrot & Netzer (2012), the widths of the narrow components are tied among different emission lines, primarily to allow a robust decomposition of the narrow and broad components that make up the Hβ emission-line profile. The FWHM of the broad Hβ line is measured from the (reconstructed) best-fit model of the broad component.

For sources with broad Hα, we use a fitting procedure that involves several progressively complicated steps, depending on the complexity of the emission lines. We start with allowing two Gaussian components for the Hα emission lines: a narrow component (with FWHM < 1000 km s^{-1}) and a broad component (FWHM > 1000 km s^{-1}), both with the wavelength centered at the Hα line. A visual inspection is made (M.K., B.T., K.O., and I.L.) to determine whether a more complex fit is required, this time using multiple Gaussians that are also allowed to be shifted. If the fit quality is still poor, we use the width of the [O III] line (from the Hβ complex fitting procedure) as an additional constraint on the narrow components in the Hα spectral region. Examples of emission-line fits are given in the Appendix.

3.3. Broad-line Black Hole Mass Measurements

For sources with broad Balmer lines, we estimated the black hole masses (M_{BH}) through virial, "single-epoch" prescriptions, which are in turn based on the R_{BLR}–L relation obtained through reverberation mapping of low-redshift AGNs (e.g., Kaspi et al. 2000; Bentz et al. 2006). The virial mass estimators we used for broad Hβ are known to suffer from systematic uncertainties of about 0.3 dex (see, e.g., Shen 2013; Peterson 2014, and references therein).

For sources with broad Hβ we used the same prescription used in Trakhtenbrot & Netzer (2012), which uses the continuum and

Table 5
Emission-line Measurements—[O II] λ3727 Spectral Region

ID[a]	FWHM[b] (km s^{-1})	[Ne V] λ3346[c] (erg cm^{-2} s^{-1})	[Ne V] λ3426[c] (erg cm^{-2} s^{-1})	[O II] λ3727[c] (erg cm^{-2} s^{-1})	[Ne III] λ3869[c] (erg cm^{-2} s^{-1})	[Ne III] λ3968[c] (erg cm^{-2} s^{-1})	Flag[d]
1	382 ± 4	⋯	⋯	1.5 ± 0.0	0.7 ± 0.0	<1.2	1
2	632 ± 55	⋯	⋯	⋯	5.5 ± 0.2	<4.7	2f
4	493 ± 2	⋯	⋯	5.5 ± 0.1	1.4 ± 0.0	<1.1	1
5	⋯	<104.0	<72.9	<24.0	<6.5	<21.2	9
6	801 ± 16	⋯	⋯	⋯	<38.0	28.9 ± 0.8	2
7	671 ± 8	⋯	⋯	13.1 ± 0.1	2.8 ± 0.0	<1.9	1
8	⋯	⋯	⋯	⋯	⋯	⋯	9
10	⋯	⋯	⋯	⋯	⋯	<1.5	2f
13	⋯	<261.4	<150.9	<45.3	<41.5	<49.5	9
14	⋯	⋯	⋯	<4.3	<7.4	<5.5	2f

Notes.
[a] *Swift*-BAT 70-month hard X-ray survey ID (http://swift.gsfc.nasa.gov/results/bs70mon/).
[b] FWHM measured from [O II] λ3727.
[c] Emission-line flux (×10^{-15}). Symbols "⋯" and "<" indicate a lack of spectral coverage and the 3σ upper limit estimation, respectively.
[d] Spectral fitting quality flag: 1—a good fit with small error, 2—acceptable fit, 3—bad fit for high S/N source due to either the presence of a broad-line component or an offset in emission lines, 9—lack of spectral coverage or no emission line is detected, f—poor calibration because a single flux calibration was applied to optical spectra taken over several different nights, as in the 6DF spectra.

(This table is available in its entirety in machine-readable form.)

Table 6
Emission-line Measurements—Narrow Hβ Spectral Region

ID[a]	FWHM[b] (km s^{-1})	He II λ4686[c] (erg cm^{-2} s^{-1})	Hβ[c] (erg cm^{-2} s^{-1})	Flag$_{bHβ}$[d]	[O III] λ5007[c] (erg cm^{-2} s^{-1})	Flag[e]
1	249 ± 1	0.3 ± 0.0	1.1 ± 0.0	n	16.1 ± 0.0	1
2	560 ± 3	<5.4	7.5 ± 0.4	n	44.6 ± 0.3	1f
4	382 ± 1	0.3 ± 0.0	1.2 ± 0.0	n	49.4 ± 0.0	1
5	1336 ± 3	<7.7	12.4 ± 0.1	n	139.6 ± 0.2	2
6	609 ± 27	⋯	82.0 ± 15.7	b	276.2 ± 6.5	1
7	637 ± 2	<0.9	4.5 ± 0.1	n	38.9 ± 0.1	1
8	416 ± 6	⋯	14.2 ± 2.7	b	181.9 ± 2.6	1
10	463 ± 98	<1.5	<2.6	n	11.0 ± 1.8	2f
13	330 ± 3	<22.5	<17.6	n	43.3 ± 1.3	1
14	506 ± 7	<5.1	<6.2	n	39.8 ± 0.3	1f

Notes.
[a] *Swift*-BAT 70-month hard X-ray survey ID (http://swift.gsfc.nasa.gov/results/bs70mon/).
[b] FWHM measured from narrow Hβ.
[c] Emission-line flux (×10^{-15}). Symbols "⋯" and "<" indicate a lack of spectral coverage and the 3σ upper limit estimation, respectively.
[d] Flag discriminating narrow Hα ("n") and broad Hα ("b"). "h" denotes a high-redshift source (see Table 10).
[e] Spectral fitting quality flag: 1—a good fit with small error, 2—acceptable fit, 3—bad fit for high S/N source due to either the presence of a broad-line component or an offset in emission lines, 9—lack of spectral coverage or no emission line is detected, f—poor calibration because a single flux calibration was applied to optical spectra taken over several different nights, as in the 6DF spectra.

(This table is available in its entirety in machine-readable form.)

line-emission parameters for virial estimates of M_{BH}:

$$M_{BH}(H\beta) = 1.05 \times 10^8 \left(\frac{L_{5100}}{10^{46}\ \mathrm{erg\ s^{-1}}}\right)^{0.65} \times \left[\frac{\mathrm{FWHM}(H\beta)}{10^3\ \mathrm{km\ s^{-1}}}\right]^2 M_\odot, \quad (2)$$

where L_{5100} is the the monochromatic luminosity at rest-frame 5100 Å, λL_λ(5100 Å), measured from the best-fit model of the Hβ region. As mentioned above, FWHM(Hβ) is measured from the entire (best-fit) broad profile. Although the fitting procedure is executed automatically for the large data set studied here, we note that we visually inspected all the Hβ fitting results (including more than one spectrum per source), and applied minor manual adjustments to provide satisfactory fits to the data. We also stress that we did not apply the Hβ-fitting code to spectra with poor absolute flux calibration (i.e., those from the 6DF survey). A summary of these fits is found in Figure 3.

For sources with broad Hα lines, we used the prescription of Greene & Ho (2005b):

$$M_{BH}(H\alpha) = 1.3 \times 10^6 \left(\frac{L_{H\alpha}}{10^{42}\ \mathrm{erg\ s^{-1}}}\right)^{0.57} \times \left[\frac{\mathrm{FWHM}(H\alpha)}{10^3\ \mathrm{km\ s^{-1}}}\right]^{2.06} M_\odot, \quad (3)$$

Table 7
Emission-line Measurements—Narrow Hα Spectral Region

ID[a]	FWHM[b] (km s^{-1})	[O I] λ6300[c] (erg cm^{-2} s^{-1})	Hα[c] (erg cm^{-2} s^{-1})	Flag$_{bH\alpha}$[d]	[N II] λ6583[c] (erg cm^{-2} s^{-1})	[S II] λ6716[c] (erg cm^{-2} s^{-1})	[S II] λ6731[c] (erg cm^{-2} s^{-1})	Flag[e]
1	221 ± 2	0.6 ± 0.0	7.6 ± 0.0	b	1.9 ± 0.0	1.4 ± 0.0	1.4 ± 0.0	1
2	510 ± 5	5.7 ± 0.3	24.4 ± 0.2	b	22.1 ± 0.3	7.8 ± 0.3	6.9 ± 0.2	2f
4	426 ± 1	1.1 ± 0.0	10.5 ± 0.0	n	5.8 ± 0.0	3.4 ± 0.0	2.5 ± 0.0	1
5	269 ± 0	1.3 ± 0.0	1.7 ± 0.1	b	1.9 ± 0.0	5.8 ± 0.0	3.9 ± 0.1	3
6	597 ± 53	<17.5	243.4 ± 6.9	b	22.9 ± 2.6	<50.8	<50.8	2
7	624 ± 1	6.8 ± 0.1	24.5 ± 0.1	n	22.6 ± 0.1	10.6 ± 0.1	9.7 ± 0.1	2
8	411 ± 0	10.9 ± 0.9	58.9 ± 0.8	b	24.3 ± 0.6	17.0 ± 0.7	14.9 ± 0.8	2
10	558 ± 70	<1.9	4.6 ± 1.5	n	3.3 ± 0.6	<2.4	<2.4	2f
13	449 ± 3	<5.7	24.0 ± 0.4	n	25.0 ± 0.2	9.2 ± 0.1	8.4 ± 0.4	1
14	506 ± 52	<5.7	12.2 ± 1.4	b	13.8 ± 2.5	4.0 ± 1.4	2.0 ± 2.2	2f

Notes.
[a] *Swift*-BAT 70-month hard X-ray survey ID (http://swift.gsfc.nasa.gov/results/bs70mon/).
[b] FWHM measured from narrow Hα.
[c] Emission-line flux (×10^{-15}). Symbols "⋯" and "<" indicate a lack of spectral coverage and the 3σ upper limit estimation, respectively.
[d] Flag discriminating narrow Hα ("n") and broad Hα ("b"). "h" denotes high-redshift source (see Table 10).
[e] Spectral fitting quality flag: 1—a good fit with small error, 2—acceptable fit, 3—bad fit for high S/N source due to either the presence of a broad-line component or an offset in emission lines, 9—lack of spectral coverage or no emission line is detected, f—poor calibration because a single flux calibration was applied to optical spectra taken over several different nights, as in the 6DF spectra.

(This table is available in its entirety in machine-readable form.)

Table 8
Strong Emission Line Classification

ID[a]	Counterpart Name	[N II]/Hα	[S II]/Hα	[O I]/Hα	He II	[O III]/[O II]
1	2MASXJ00004876−0709117 (B)[b]	Seyfert	Seyfert	Seyfert	Seyfert	Seyfert
2	Fairall1203 (B)	Seyfert	Seyfert	Seyfert	No He II detection	⋯[c]
4	2MASXJ00032742+2739173	Seyfert	Seyfert	Seyfert	Seyfert	Seyfert
5	2MASXJ00040192+7019185 (B)	Optically elusive	Optically elusive	Optically elusive	Optically elusive	Optically elusive
6	Mrk335 (B)	H II	Optically elusive	Optically elusive	Seyfert	Optically elusive
7	2MASXJ00091156−0036551	Seyfert	Seyfert	Seyfert	No He II detection	Seyfert
8	Mrk1501 (B)	Seyfert	Seyfert	Seyfert	Seyfert	⋯
10	2MASXJ00210753−1910056	AGN Limit[d]	Optically elusive	Optically elusive	No He II detection	Optically elusive
13	2MASXJ00253292+6821442	AGN Limit	AGN Limit	Optically elusive	No He II detection	⋯
14	2MASXJ00264073−5309479 (B)	AGN Limit	AGN Limit	Optically elusive	No He II detection	Optically elusive

Notes.
[a] *Swift*-BAT 70 month hard X-ray survey ID (http://swift.gsfc.nasa.gov/results/bs70mon/).
[b] The symbol (B) indicates a broad-line source.
[c] The symbol ⋯ indicates a lack of wavelength coverage, in reference to the "no wave" classification listed in Figures 10 and 11.
[d] AGN Limit refers to objects that have an Hβ upper limit either in the Seyfert or in the LINER region.

(This table is available in its entirety in machine-readable form.)

where $L_{H\alpha}$ is the integrated luminosity of the broad component of the Hα line, determined from the best-fitting model. This prescription is therefore mostly unaffected by host light. Since the Hα-related prescription (Equation (3)) is based on a *secondary* calibration of a R_{BLR}–L(Hα) relation, it carries somewhat larger systematic uncertainties (compared with the Hβ-based one). However, it can be applied to Seyfert 1.9 AGNs without broad Hβ lines and it may perform better for sources that have high levels of stellar contamination and/or extinction. A summary of the results of the fitting is provided in Figure 4. We found that about a quarter of Seyfert 1.9 (27%, 31/116) have weak broad Hα lines (EW < 50 Å; see the general discussion of Seyfert sub-classes in Section 4.2). More details on these objects are given in the Appendix.

For 19 high-redshift sources ($z \sim 1$–3.3), the available optical spectra include either the Mg II λ2798 or C IV λ1549 broad emission lines. The emission complexes around these two lines were fitted using dedicated procedures, described in detail in Trakhtenbrot & Netzer (2012, see Appendices C2 and C3 therein). These take into account the (blended) emission features from iron and He II λ1640 transitions (in the case of Mg II and C IV, respectively). For both broad lines, each of the doublet features is modeled with two broad Gaussians. We assume no narrow-line contribution to these transitions (see Trakhtenbrot & Netzer 2012, and references therein).

We used the best-fit models of the broad emission lines, together with the adjacent continuum luminosities, to estimate M_{BH} in these 19 high-redshift sources. For the Mg II line, we used the prescription presented by Trakhtenbrot & Netzer (2012), which is calibrated against Hβ-based mass estimates using a larger sample of SDSS quasars for which both lines are available. An identical prescription was also independently derived by Shen et al. (2011). For the C IV line, we used the

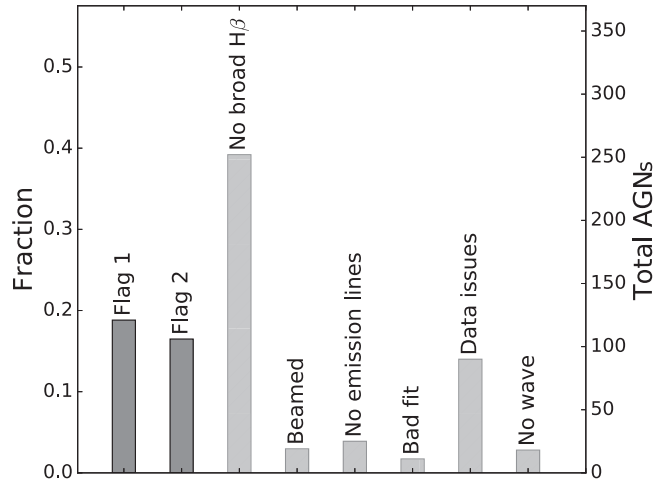

Figure 3. Summary of broad-line Hβ black hole mass measurements using the fitting procedure described by Trakhtenbrot & Netzer (2012), which includes fitting Fe II lines. For 35% (225/642), we have a measurement of black hole mass using broad Hβ lines. "Flag 1" represents an excellent fit based on visual inspection. "Flag 2" spectra have a good fit based on visual inspection. The remaining categories (dashed histograms) have features that prevented measurements. "Beamed AGNs" are sources that are known to be beamed and lack emission lines. "No emission lines" indicates the galaxy has a high quality spectra but no Balmer lines are detected. "No wave" indicates sources with typically high redshift that lack coverage of Hβ. Finally, small fraction of the data were low-quality or a very poor fit was obtained.

prescription presented by Vestergaard & Peterson (2006). We note that C IV-based estimates of $M_{\rm BH}$ are known to be considerably less reliable (e.g., Denney 2012) than those based on lower-ionization transitions, perhaps due to significant contributions from non-virialized BLR gas motion to the emission-line profile (see detailed discussion in Trakhtenbrot & Netzer 2012, and references therein). We therefore advise that the C IV-based determinations of $M_{\rm BH}$ provided here may carry large uncertainties and possibly systematic biases. At such high redshifts, however, they provide the only estimate of $M_{\rm BH}$, in lieu of NIR spectroscopy of the other emission lines.

The spectral and derived parameters of the 19 high-redshift sources are listed in Table 10. We finally note that the *Swift*-BAT sample of AGNs probably includes several other high-redshift (and therefore high-luminosity) sources, for which an optical spectrum is not available within the large optical surveys we use, and/or the effects of beaming are not yet well understood. We plan to address this population in a separate publication.

3.4. Bolometric Luminosity

We estimated the bolometric luminosity of the AGNs in our sample ($L_{\rm bol}$) from the observed X-ray luminosity measured by the *Swift*-BAT survey in the energy range 14–195 keV. First, we divided the 14–195 keV luminosity by 2.67 to convert to the intrinsic 2–10 keV luminosity, following Rigby et al. (2009), which is based on scaling the Marconi et al. (2004) templates to higher X-ray energies. We then used the median bolometric correction from Vasudevan et al. (2009) of the BAT sample, which resulted in a factor of 8 difference between $L_{\rm bol}$ and $L_{14-195{\rm keV}}$. More advanced luminosity-dependent bolometric corrections will be examined in future studies.

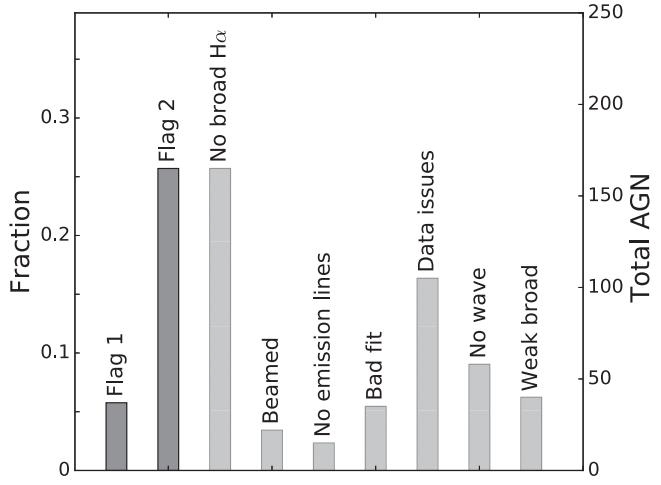

Figure 4. Summary of broad-line Hα black hole mass measurements. For 38% (242/642), we have a measurement of black hole mass using broad Hα lines. The categories are the same as in Figure 3.

4. Results

In this section we present the X-ray luminosity using our new measurements of redshifts (Section 4.1). We proceed with AGN classification based on the narrow and broad lines, and then compare it with the classification of unobscured sources based on X-ray data (i.e., using the column density $N_{\rm H}$; Section 4.2). Next, we provide optical emission-line classifications for all the AGNs in the survey (Section 4.3). We then compare our demographics of BASS X-ray-selected AGNs to SDSS-selected AGNs (Section 4.4). We also present the distributions of black hole masses, bolometric luminosities, and accretion rates (Section 4.5). Finally, we discuss the variety of unusual AGNs we have identified in this large survey (Section 4.6).

4.1. Redshift Distribution

We begin by showing a plot of the X-ray luminosities in the entire *Swift*-BAT AGN sample, using our new redshift measurements or those from NED when the spectra are not available (Figure 5). We also show several other, deep X-ray surveys, for comparison. The majority (≈90%) of BAT-detected AGNs are nearby ($z < 0.2$). Their X-ray luminosities are similar to AGNs found in deeper surveys because of the larger survey area. Our survey finds 46 new redshifts for sources without measurements in NED. This leads to a redshift completeness of 96% (803/836) for the 70-month BAT AGN catalog. The newly measured sources are at similar redshifts (median $z = 0.049$) to the sources in the rest of the sample (median $z = 0.038$). A summary of the spectroscopic coverage is in Figure 6.

Only three sources with redshifts measured in BASS show significant differences from those in NED. QSO B0347-121 is listed at $z = 0.18$ in NED; however, our measurements of the 6DF spectrum clearly show emission lines at $z = 0.032$, in agreement with the redshift tabulated in the 6DF catalog. ESO 509-IG 066 NED02 is listed in NED as $z = 0.0446$; however, our measurements of the 6DF spectrum clearly show emission lines at $z = 0.034$, again in agreement with the 6DF catalog. 1RXS J090915.6+035453 is listed as $z = 3.20$ in NED, but the lines are clearly redshifted to $z = 3.28$ based on our

Table 9
Properties Derived from Spectral Decomposition of Broad Hβ and Hα Sources

ID[a]	$\log L_{5100}$ (erg s^{-1})	$\log L_{\rm bol}$[b] (erg s^{-1})	FWHM$_{bH\beta}$ (km s^{-1})	EW$_{bH\beta}$ (Å)	$\log M_{\rm BH}/M_\odot$[c]	$\log L/L_{\rm Edd}$[c] 5100 Å	Flag$_{bH\beta}$[d]	bHα[d] (erg cm^{-2} s^{-1})	FWHM$_{bH\alpha}$ (km s^{-1})	EW$_{bH\alpha}$ (Å)	$\log M_{\rm BH}/M_\odot$[e]	Flag$_{bH\alpha}$[f]	$\log L/L_{\rm Edd}$[g]	$\log(M_{\rm BH}/M_\odot)_{\rm lit.}$[h]
1	…	…	…	…	…	…	…	9.5 ± 0.1	3680 ± 25	14.79	6.42	1	−0.00	…
6	43.90	44.80	2065	99.42	7.29	−0.67	1	1929.3 ± 8.7	1706 ± 669	297.48	6.86	2	−0.61	$7.23^{+0.04}_{0.04}$
8	44.43	45.28	5295	100.66	8.45	−1.34	1	1076.6 ± 2.0	4704 ± 33	492.98	8.26	2	−0.67	$8.07^{+0.17}_{0.12}$
16	44.66	45.50	2451	69.27	7.93	−0.61	1	…		…	…	…	…	$8.49^{+0.12}_{0.10}$
18	…	…	…	…	…	…	…	319.3 ± 1.9	11519 ± 66	421.97	8.84	2	−1.46	…
28	…	…	…	…	…	…	…	53.7 ± 0.3	5469 ± 110	18.83	6.93	2	−0.42	…
33	…	…	…	…	…	…	…	110.2 ± 1.2	2010 ± 26	35.70	6.02	1	0.66	…
36	43.43	44.37	5446	133.99	7.82	−1.63	1	…		…	…	…	…	…
39	44.74	45.58	5205	126.00	8.64	−1.24	1	…		…	…	…	…	$8.46^{+0.09}_{0.08}$
43	42.83	43.85	4214	57.64	7.21	−1.54	2	491.4 ± 4.2	3536 ± 1881	225.14	6.90	2	−0.93	…

Notes.
[a] *Swift*-BAT 70-month hard X-ray survey ID (http://swift.gsfc.nasa.gov/results/bs70mon/).
[b] $L_{\rm bol}$ is estimated from L_{5100}, following Trakhtenbrot & Netzer (2012).
[c] Following Trakhtenbrot & Netzer (2012), with $L_{\rm bol}$ estimated from L_{5100}.
[d] Spectral fitting quality flag for broad Hβ: 1—a good fit with small error, 2—acceptable fit.
[e] Black hole mass derived from broad Hα following Greene & Ho (2005b).
[f] Spectral fitting quality flag for broad Hα: 1—a good fit with small error, 2—acceptable fit.
[g] Eddington ratio derived from the *Swift*-BAT survey (14–195 keV) and $M_{\rm BH}$ following Greene & Ho (2005b).
[h] Black hole mass from Bentz & Katz (2015, http://www.astro.gsu.edu/AGNmass/).

(This table is available in its entirety in machine-readable form.)

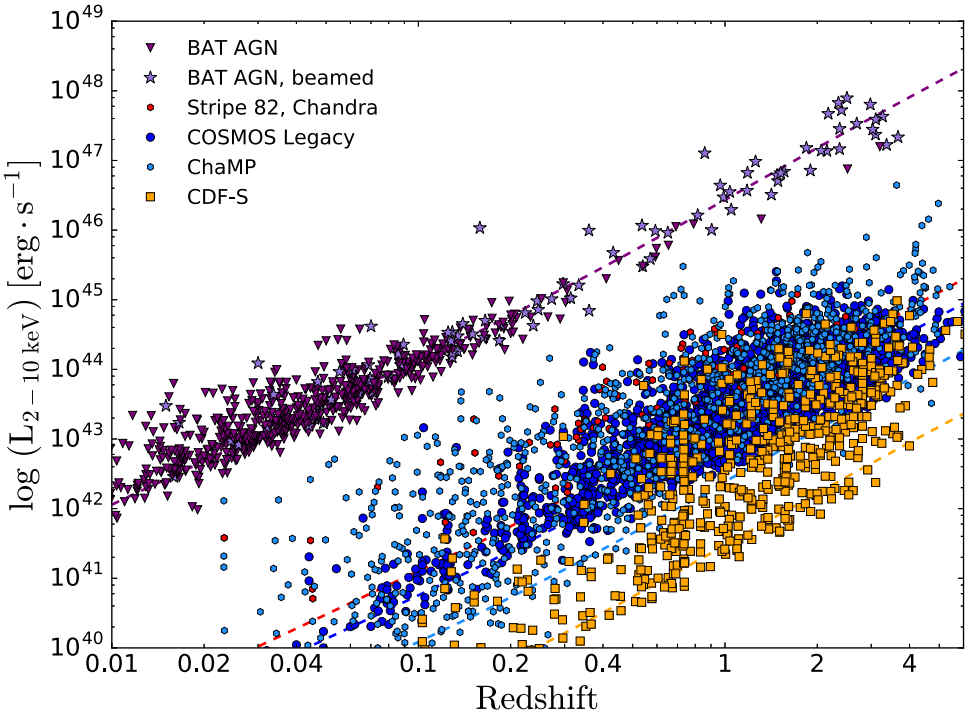

Figure 5. Distribution of the rest-frame hard X-ray luminosity based on the 14–195 keV emission of the BAT AGNs. We used a ratio of 2.67 (Rigby et al. 2009) to estimate the 2–10 keV luminosity from the 14 to 195 keV luminosity. We have included other deeper X-ray surveys for comparison ((Xue et al. 2011; Trichas et al. 2012; Civano et al. 2016; Lamassa et al. 2016; Marchesi et al. 2016). For other X-ray surveys, we have assumed $\Gamma = 1.5$ to estimate the intrinsic luminosity for obscured and unobscured X-ray sources. The BAT AGN redshifts are measured from BASS using narrow emission lines, or NED when no spectra are available. The red dashed line shows the flux limit of BAT over 90% of the sky (1.34×10^{-11} erg cm^{-2} s^{-1}). The unbeamed AGNs in the BASS sample tend to span the moderate- to high-luminosity end of the X-ray luminosity function (XLF) at all redshifts. Samples from deeper published surveys, such as the *Chandra* Deep Field South (CDF-S), tend to sample a lower-luminosity range of the X-ray luminosity function.

Table 10
Properties Derived from Spectral Decomposition of High-redshift Sources

ID[a]	Counterpart Name	Redshift	Line[b]	$\log L_{\rm cont.}$[c] (erg s^{-1})	$F_{\rm line}$[d] (erg cm^{-2} s^{-1})	EW$_{\rm line}$ (Å)	FWHM$_{\rm line}$ (km s^{-1})	$\log M_{\rm BH}/M_{\odot}$	$\log L/L_{\rm Edd}$	Flag[e]
120	[HB89]0212+735	2.367	C IV	46.26	6.02	21.13	8207	9.69	−0.89	2
188	4C+32.14	1.258	Mg II	46.26	12.19	13.56	2790	9.04	−0.46	1
311	[HB89]0552+398	2.365	C IV	46.04	2.46	15.11	3134	8.74	−0.16	1
387	B2 0743+25	2.994	C IV	46.24	3.66	26.81	5689	9.36	−0.58	2
428	[HB89]0836+710	2.172	C IV	46.75	15.36	16.18	7754	9.90	−0.61	1
445	1RXS J090915.6+035453	3.288	C IV	46.30	3.36	25.64	6000	9.43	−0.60	1
545	PKS1127−14	1.184	Mg II	45.65	3.74	18.26	3208	8.78	−0.79	1
601	B2 1210+33	2.504	C IV	46.30	9.44	38.44	4299	9.15	−0.31	2
645	3C279	0.536	C IV	45.11	20.74	27.27	6196	8.83	−1.19	2
693	LBQS 1344+0233	1.310	Mg II	45.89	6.55	23.24	2326	8.65	−0.43	1
752	3C309.1	0.905	Mg II	45.27	9.15	52.32	3374	8.59	−0.93	2

Notes.
[a] *Swift*-BAT 70-month hard X-ray survey ID (http://swift.gsfc.nasa.gov/results/bs70mon/).
[b] Broad emission line (C IV λ1549 or Mg II λ2798) fitted to measure spectral quantities listed in this table.
[c] Monochromatic luminosity at rest-frame 1450 Å (C IV λ1549) or 3000 Å (Mg II λ2798).
[d] Emission-line flux ($\times 10^{-15}$).
[e] Spectral fitting quality flag: 1—a good fit with small error, 2—acceptable fit.
(This table is available in its entirety in machine-readable form.)

measurements, and in agreement with the SDSS catalog measurement.

4.2. Narrow- and Broad-line Classification

We first classify the BAT AGNs depending on the presence and strength of broad emission lines (e.g., Osterbrock 1981). A Seyfert 1.9 classification is a source with a narrow Hβ line and broad Hα line. We use the quantitative classifications for Seyfert sub-classes (1, 1.2, 1.5, and 1.8) based on Winkler (1992), using the total flux of [O III] and Hβ. A summary of the results of this classification can be found in Figure 7. About half of the sources are Seyfert 2 or Seyfert 1.9, and about a quarter are Seyfert 1.2 and 1.5. A small fraction are true Seyfert 1 (7%) and only two are Seyfert 1.8 sources.

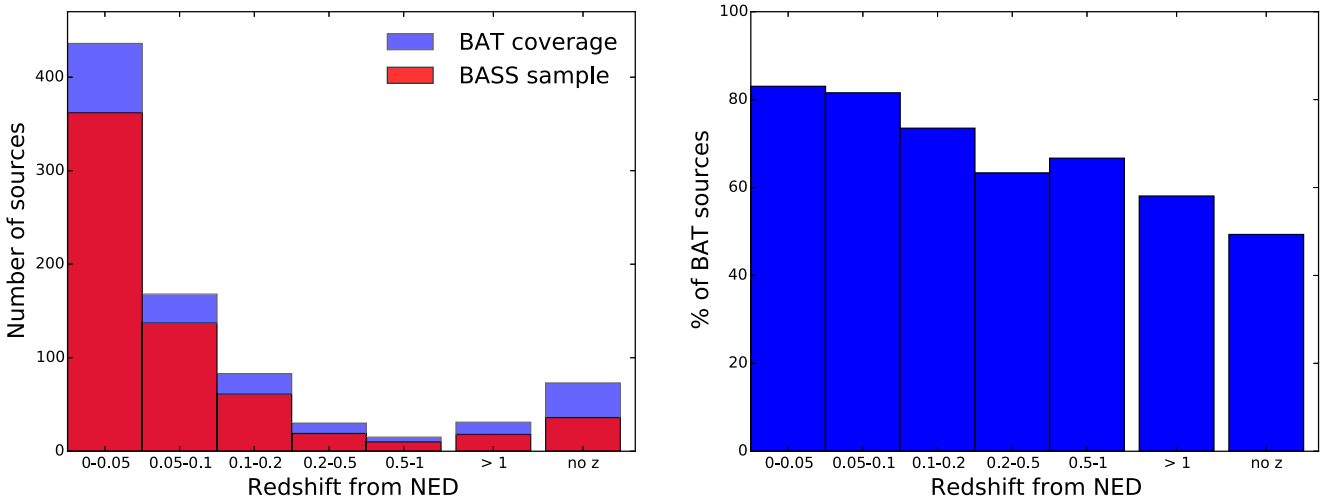

Figure 6. Summary of spectroscopic coverage with redshift for the BASS sample. Left: number of sources with spectra (red) compared to the number of AGNs in the BAT catalog (blue) at different redshift intervals based on NED. The right panel shows the percentage of BAT AGNs covered by the BASS sample in redshift intervals. The majority of the spectra are low-redshift ($z < 0.05$), consistent with the BAT sample. The spectroscopic completeness is 75%, but falls with increasing redshift because of the increasing fraction of faint sources and beamed sources.

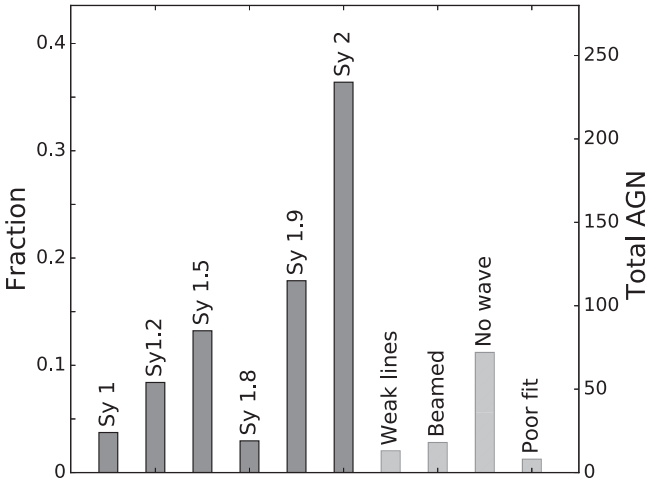

Figure 7. Dichotomy of BAT AGNs depending on the presence and strength of broad emission lines. For 84% of spectra (539/642), we have measurements of Seyfert types. A Seyfert 1.9 classification is a source with a narrow Hβ line and broad Hα line. The remaining categories (dashed histograms) have features that prevented measurements. "Weak lines" refers to objects without the presence of any Balmer emission lines in the spectra, despite high-quality spectra. We use the quantitative classifications for Seyfert types (1, 1.2, 1.5, 1.8) based on Winkler (1992) using the total flux of [O III] and Hβ.

We compare our Seyfert types (Sy 1, Sy 1.2, Sy 1.5, Sy 1.8, Sy 1.9, and Sy 2) to the most recent 13th edition Veron-Cetty catalog of AGNs (Veron-Cetty & Veron 2010). Only a minority (36%, 230/642) of the BASS sample is classified in this catalog by Seyfert type. Using this subsample of 230 we find that the majority, 89% (206/230), agree with the Seyfert type classification with the Veron-Cetty catalog. These include 77% (177/230) that show exact type agreement or are listed as a unspecified Sy 1 in the Veron-Cetty catalog and found to be Sy 1, Sy 1.2, Sy 1.5, or Sy 1.9 in BASS. Another 13% (29/230) are Sy 1, but are listed as Sy 1.2 or Sy 1.5 and vice versa in BASS.

The remaining 10% (24/230) show disagreement among Seyfert type between BASS and Veron-Cetty. The majority of these are listed as Sy 1.9 in our sample but are found to be Sy 2 in Veron-Cetty 67% (16/24), most likely because our of higher-quality spectra. There are no examples of Sy 1.9 in the Veron-Cetty catalog that are found to be Sy 2 in our catalog.

Another six sources are Sy 1 unspecified in Veron-Cetty, but Sy 2 in our catalog. For PKS 0326-288, the Veron-Cetty reference (Mahony et al. 2011) lists the source as a narrow-line source in agreement with our classification. MCG +02-21-013 has no references in the Veron-Cetty catalog for the Seyfert type, but NED lists both a Sy 1 and Sy 2 in agreement with our classification. NGC 4992 has no references in the Veron-Cetty catalog for the Seyfert type, but is classified as a Sy 2 in a recent paper by Smith et al. (2014) in agreement with our classification. A recent paper on MCG+04-48-002 (Koss et al. 2016b) lists it as a Sy 2, in agreement with our classification, while it has no references in the Veron-Cetty catalog for the Seyfert type. NGC 5231 is listed as a Sy 2 to match our classification in recent work (Parisi et al. 2012). Finally, 2MASX J10084862–0954510 is shown to be an Sy 1 in Bauer et al. (2000), with broad Balmer lines, which is very different from our spectra and may be a case of variability.

Finally, two sources are listed as Sy 1.0 in Veron-Cetty, but are listed as Sy 1.9 in the BASS catalog. The reference for ESO 198-024 as a Sy 1.0 in Veron-Cetty is based on imaging variability (Winkler et al. 1992) in the optical rather than spectroscopy, and could be consistent with our Sy 1.9 classification. Finally, the reference in Veron-Cetty for a Sy 1.0 classification (Guainazzi et al. 2000) lists the source as a Sy 1.9, which is the same as our classification, though the authors mention the source may have changed from a narrow-line AGN to a Sy 1.9.

In summary, we find broad agreement (89%) with past studies of Seyfert type classification from the Veron-Cetty catalog. The major difference is that 16 sources in the BASS catalog are now classified as Sy 1.9 because of broad lines detected in Hα for the first time. Finally, eight sources show a different Seyfert type, possibly due to variability, which will be further studied in future publications.

In Figure 8 we present the fraction of sources with broad Hα and/or Hβ lines, plotted against X-ray luminosity. For both the 14–195 keV and 2–10 keV luminosities we find a general increase in type 1 fraction with increasing luminosity, as has

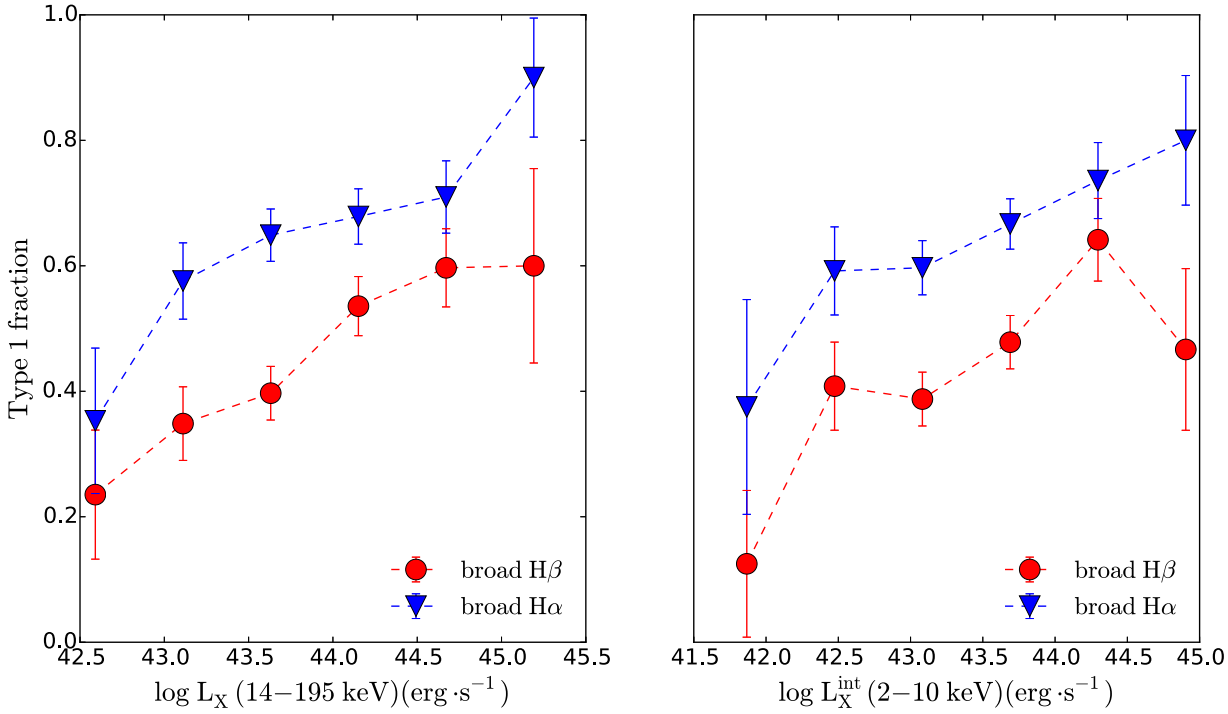

Figure 8. Fraction of AGNs classified as Type 1, based on the presence of broad Balmer lines, vs. X-ray luminosity (14–195 keV in the left panel, and 2–10 keV in the right one). Error bars are calculated using the binomial distribution. There is a general increase in the fraction of broad-line AGNs with X-ray luminosity, using both Hα and Hβ.

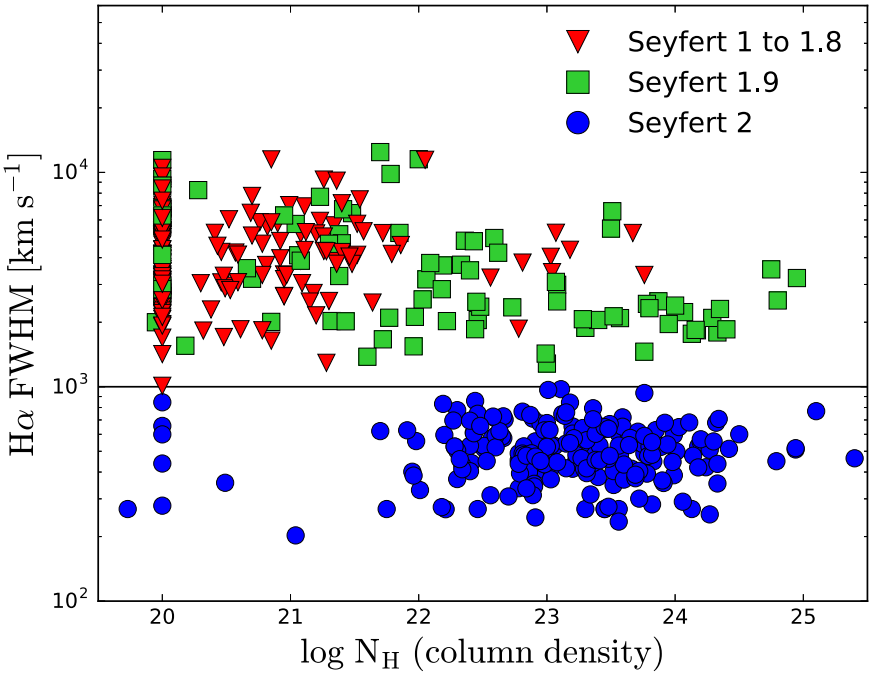

Figure 9. FWHM of Hα as a function of column density. Colors represent the Osterbrock classification. In the sample, 128 Seyfert 1 to 1.8 and 36 Seyfert 1.9 s have a column density consistent with a lower limit ($N_H = 10^{20}$ cm^{-2}). We note that there are only two Seyfert 1.8 in the sample, so the broad-line sample is dominated by Seyfert 1–1.5 types. We find a general agreement between the X-ray column density and the presence of broad lines with $N_H < 10^{22}$ cm^{-2} as a dividing line between most type 1 and type 2 sources. However, Seyfert 1.9 show the full range of column densities.

been found in past studies using broad Hβ (see, e.g., Merloni et al. 2014, and references therein). We find that AGNs with broad Hα lines are consistently more common, by about 10%–20%, than AGNs with Hβ lines, across a wide range of X-ray luminosity.

Finally, in Figure 9 we plot the FWHM of Hα as a function of the column density derived from the X-rays (N_H). We note that roughly half (57%, 128/223) of Seyfert 1–1.8 broad-line AGNs with column density measurements have only upper limits on N_H at 10^{20} cm^{-2}, corresponding to being unobscured.

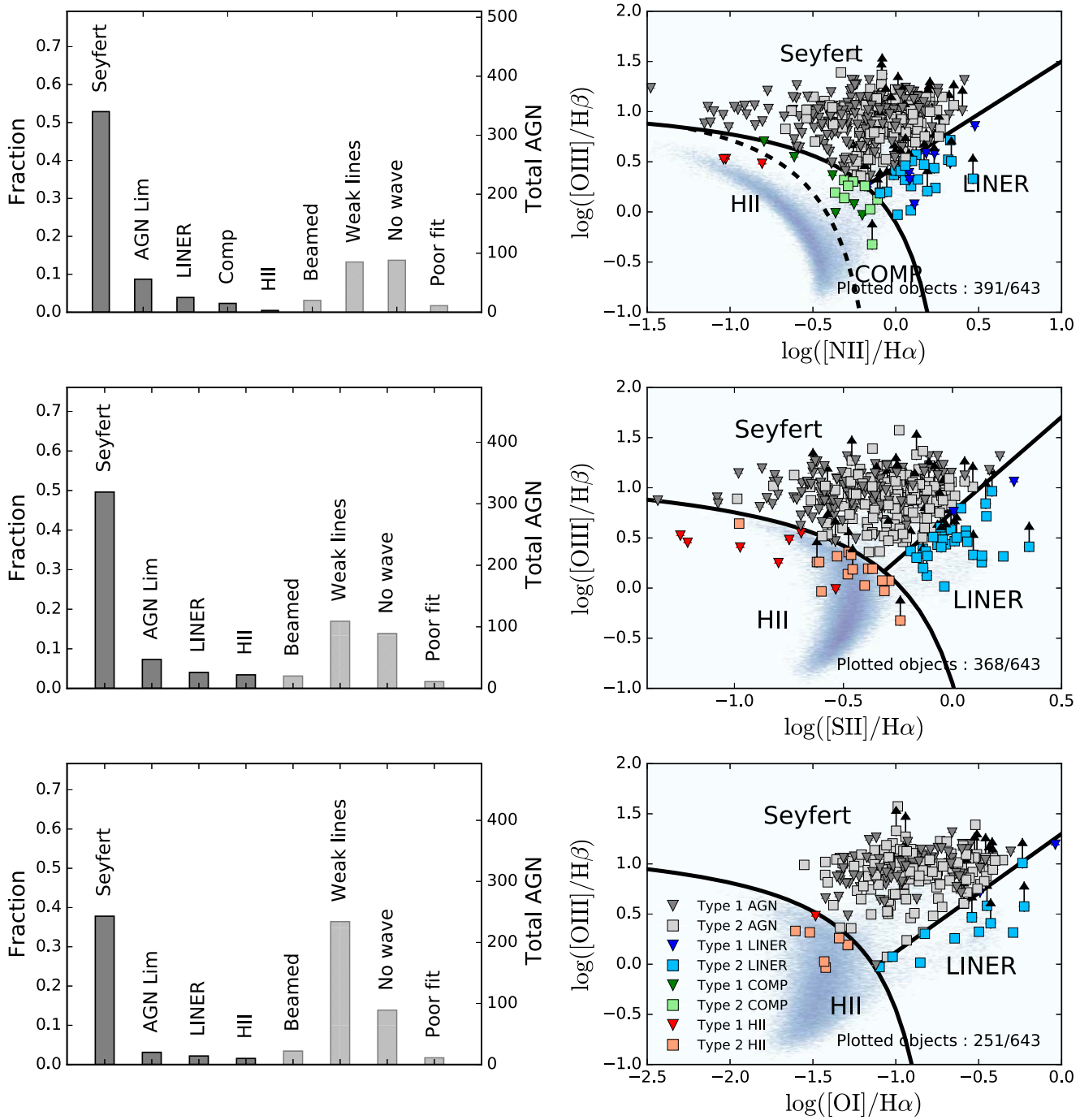

Figure 10. Classification of the sample using line diagnostics diagrams (Kewley et al. 2006). Left column: histograms for the entire sample. "AGN lim" refers to objects that have an Hβ upper limit either in the Seyfert or in the LINER region. The remaining categories (dashed histograms) have features that prevented measurements. "Weak lines" refers to objects with high S/N spectra that lack sufficiently strong emission-line measurements to be placed on the diagram. "Beamed AGN" refers to any sources cross-matched to the blazar and beamed AGN catalogs. We note that most beamed AGNs in our sample are not blazars and have emission lines and are classified using emission-line diagrams. "Poor fit" refers to AGNs with complex emission-line profiles that were poorly fit using our automated routine. Finally, "no wave" refers to objects lacking sufficient wavelength coverage to measure the needed emission lines. Right Column: line diagnostic diagrams for sources with sufficient measurable emission lines to be classified using line diagnostic diagrams. The gray area represents the distribution of the SDSS sample. Narrow-line objects are shown with squared and broad-line objects (broad Hβ detection) with triangles. The arrows represent upper limits and lower limits. We find good agreement between all three classical line diagnostic diagnostics in the fraction of Seyferts, LINERS, composite galaxies, and H II regions with [N II] λ6583 showing the largest number of line measurements and [O I] λ6300 showing the fewest.

The FWHMs of the emission lines show broad agreement with the X-ray obscuration (~94%), such that Seyfert sub-types 1, 1.2, 1.5, and 1.8 have $N_{\rm H} < 10^{21.9}$ cm^{-2}, and Seyfert 2 have $N_{\rm H} > 10^{21.9}$ cm^{-2}. Seyfert 1.9, however, show a range of column densities.

Additionally, a small fraction of Seyfert 2 sources (6%, 14/221) have X-ray obscuration below $N_{\rm H} = 10^{21.9}$ cm^{-2}. We note, however, that Seyfert 1.9 sources, which have evidence of a broad-line in Hα, but not Hβ, span the full range of column densities from unobscured to Compton-thick (i.e., $N_{\rm H} < 10^{24}$ cm^{-2}).

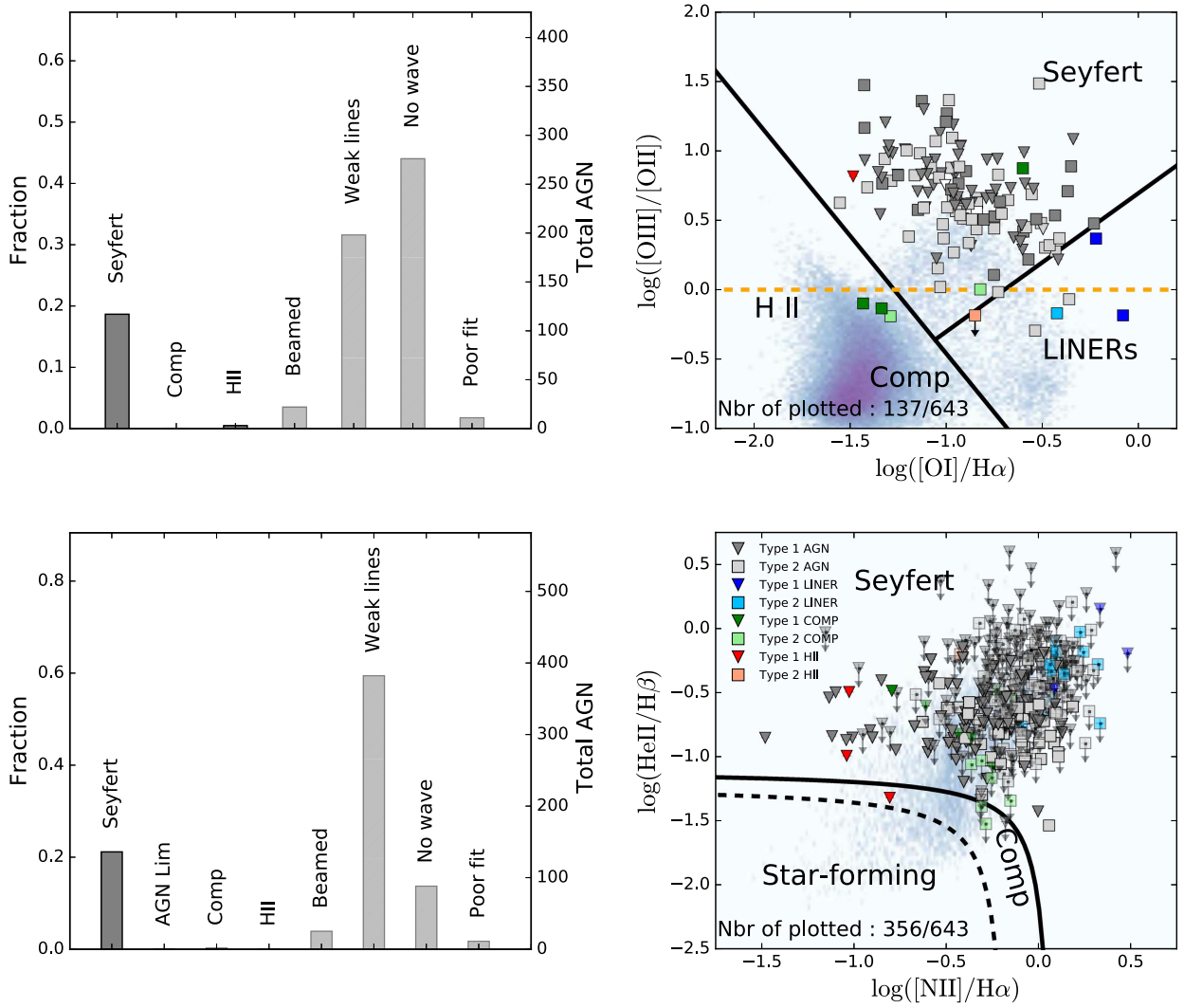

Figure 11. Classification of the sample using the [O III] λ5007/[O II] λ3727 vs. [O I] λ6300/Hα and He II λ4686/Hβ vs. [N II] λ6583/Hα diagnostic diagrams (Shirazi & Brinchmann 2012) using the same scheme as the previous line diagnostic figure. Compared to the traditional diagnostics ([N II] λ6583, [S II] λ6717,6731, and [O I] λ6300), these two diagnostics fail to classify the majority objects because of the difficulty detecting the He II λ4686 line and the lack of blue coverage in most spectra for the [O II] λ3727 line.

4.3. Emission-line Classification

We use the emission-line diagnostics of Veilleux & Osterbrock (1987), revised by Kewley et al. (2006). We classify each AGN using the [O III] λ5007/Hβ versus [N II] λ6583/Hα, [S II] λ6717, 6731/Hα, and [O I] λ6300/Hα diagnostics (Figure 10). For the [N II] λ6583 diagnostic, we further separate the star-forming (H II) galaxies and composite galaxies, and separate AGNs into LINERs and Seyferts (following Schawinski et al. 2007b). Finally, we also apply the [O III] λ5007/[O II] λ3727 and He II λ4686/Hβ diagnostics, defined by Shirazi & Brinchmann (2012).

We find that roughly half of BAT AGNs are found in the Seyfert region of the [N II] diagram (53%, 338/642). The next largest sub-group is sources without an Hβ detection (4%, 338/642), though the detection limits imply either a Seyfert or LINER AGN classification. About 15% of sources have weak lines, and despite high-S/N optical spectra, lack enough emission-line measurements for line diagnostic diagrams. The remaining categories of LINERs, composite galaxies, and H II classifications are rare, with only a few percent of BAT AGNs found in each. A few percent of sources also have complex emission-line profiles where a good fit to the emission lines was not obtained. Finally, about 10% of sources lack sufficient wavelength coverage, because of the instrumental setup or their high redshifts.

The [S II] λ6717,6731 diagnostic shows a very similar distribution, though there is a slightly lower fraction of Seyferts (50%, 317/642), due to the weaker [S II] line (and limited S/N of the data), and a larger fraction of H II regions. For the [O I] diagnostic, the line is markedly weaker than the [N II] and [S II] line, and therefore identifies somewhat fewer Seyferts (38%, 242/642), and has about double the number of sources that lack emission-line detection. For sources with line detections in all three diagnostics (35%, 225/642), we find good agreement in the AGN classification across the diagnostics (81%, 182/225).

We also classify the sample using the [O III] λ5007/[O II] λ3727 versus [O I] λ6300/Hα and He II λ4686/Hβ versus& [N II] λ6583/Hα diagnostic diagrams (Figure 11). Compared to the more commonly used diagnostics (i.e., [N II], [S II], and [O I]), these two diagnostics are not efficient for classifying the majority of AGNs in our sample, because of the difficulty in

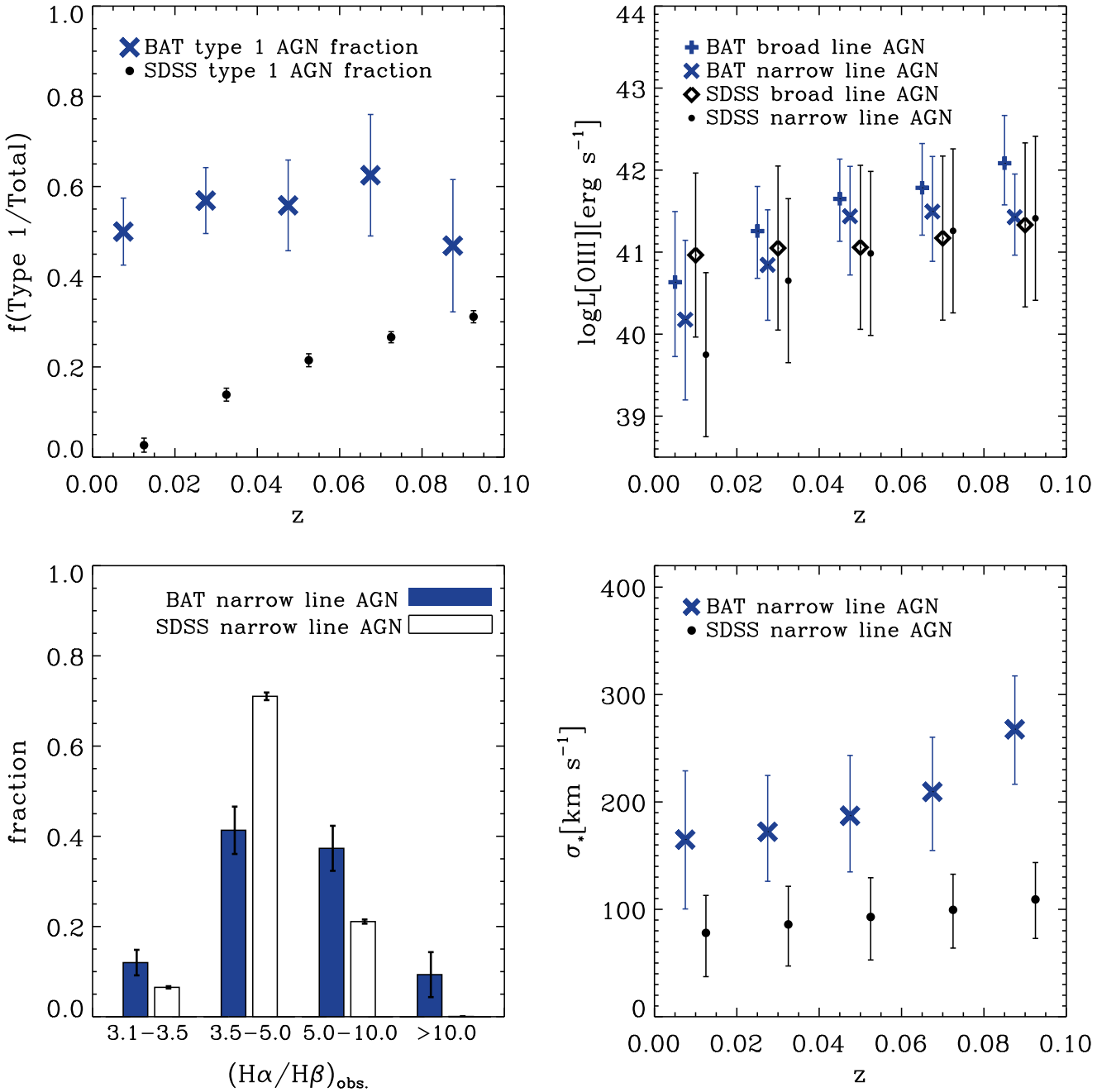

Figure 12. Comparison of BASS X-ray-selected AGNs to optically selected Seyferts in the SDSS from the OSSY catalog (Oh et al. 2011). Median and 1σ distribution are shown with 0.02 redshift bins. Upper left: Type 1 AGN fraction vs. redshift. The BASS sample is fairly constant with redshift, whereas the SDSS evolves strongly. Upper right: [O III] luminosity vs. redshift. The type 1 AGNs and type 2 AGNs in BASS have higher [O III] luminosities than SDSS AGNs. Bottom left: Balmer decrement compared to the SDSS narrow-line AGN sample. Narrow-line, BAT-detected AGNs have a larger fraction of AGNs in dustier galaxies (Hα/Hβ > 5). Bottom right: velocity dispersion vs. redshift. BAT AGNs tend to have larger velocity dispersions than SDSS-selected AGN, consistent with the fact that the SDSS Seyfert 2 AGN sample is 30 times larger than the BAT AGN.

detecting the He II line and the lack of blue coverage in most spectra for the [O II] line.

4.4. Comparison to Optical Emission-line-selected AGNs from the SDSS

We perform a comparison of the demographics of the BASS X-ray-selected AGNs to optically selected Seyferts in the SDSS, based on the OSSY catalog (Oh et al. 2011, 2015). The results are shown in Figure 12. We find that the BASS X-ray-selected AGNs show a relatively constant type 1 to type 2 fraction of ∼55% over the redshift range of $z < 0.1$, while the fraction in SDSS AGNs is much lower and furthermore shows a strong dependence on redshift (2%–30%).[23] The [O III] luminosities of BAT AGNs are higher, on average, than those of SDSS AGNs, for both Seyfert 1 and Seyfert 2 AGNs. The BASS narrow-line AGNs show a larger number of sources with high

[23] The OSSY catalog classifies AGNs as type 1 or type 2 solely based on the presence of a broad Hα emission line (see details in Oh et al. 2015).

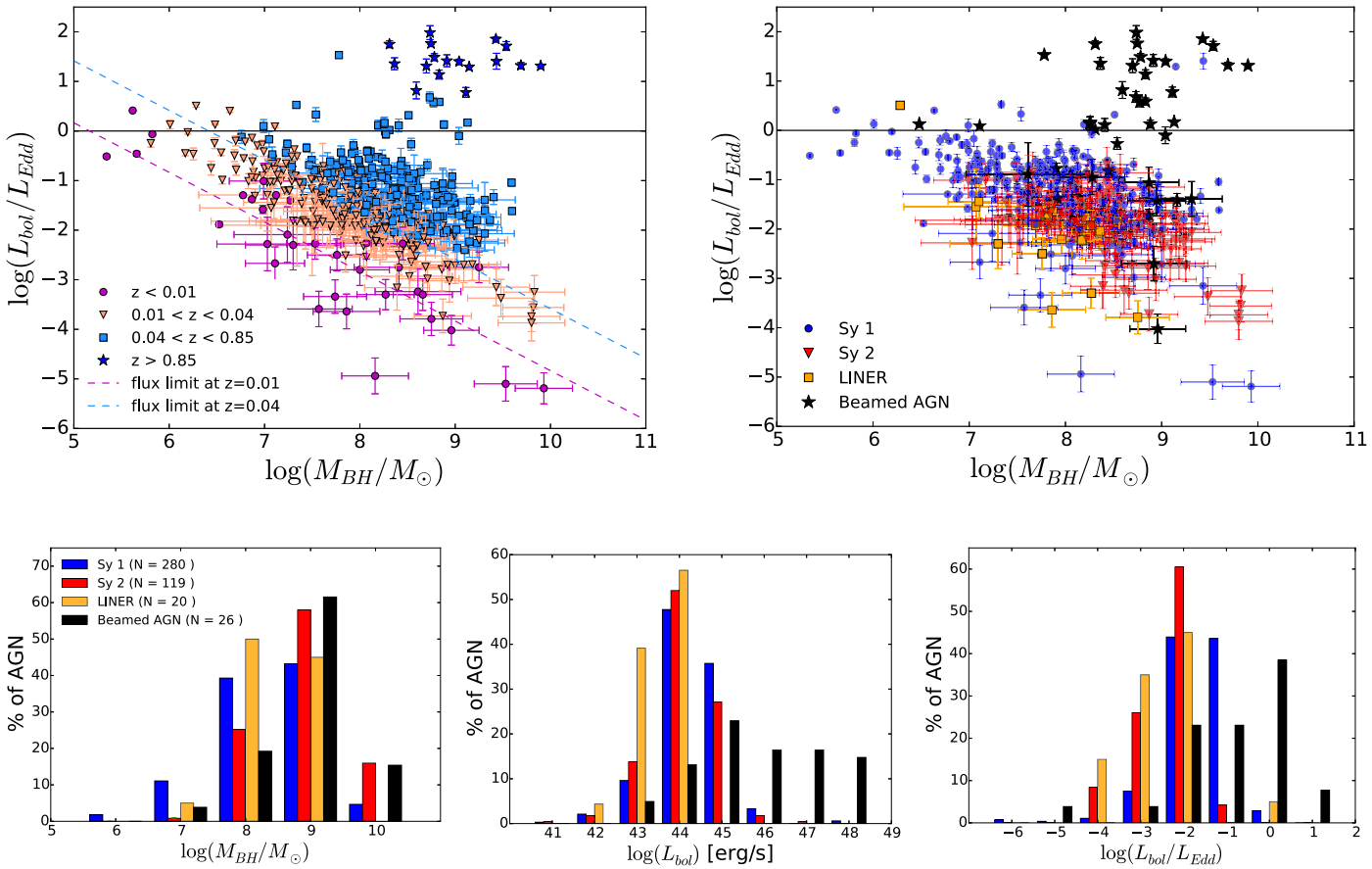

Figure 13. Top left panel shows the distribution of AGN Eddington ratio ($L/L_{\rm Edd}$) and black hole mass ($M_{\rm BH}$) with redshift. The top right panel shows the distribution of the Eddington ratio and black hole mass with AGN type. The bottom panels show histograms of black hole mass (left), bolometric luminosity (center), and Eddington ratio (right) with AGN type.

Balmer decrements (Hα/H$\beta > 5$), compared to SDSS AGNs. This can be clearly understood by the requirement to have robust detections of all relevant emission lines for SDSS AGNs to be classified as such, which the hard X-ray selection of BASS AGNs overcomes. Finally, the average stellar velocity dispersions of the BAT narrow-line AGNs (191 ± 17 km s^{-1}) are significantly higher than those of narrow-line SDSS AGNs (101 ± 10 km s^{-1}), and show a stronger redshift dependence.

4.5. Black Hole Mass and Accretion Rate Distribution

Using the black hole mass estimated from velocity dispersion and broad Balmer lines, we find that the black hole masses of our BASS AGNs range between $10^{5.4}$ and 10^{10} $M_\odot$. Figure 13 shows the distribution of $M_{\rm BH}$ in different redshift ranges and for Seyfert 1–1.9, Seyfert 2, LINERs, and beamed AGNs.

We use the median and median absolute deviation (MAD) to compare the populations because of the spread over several orders of magnitude. The median and MAD are $M_{\rm BH} = (5.8 \pm 8.5) \times 10^7\,M_\odot$ for $z < 0.01$, $M_{\rm BH} = (6.4 \pm 8.1) \times 10^7\,M_\odot$ for $0.01 < z < 0.04$, and $M_{\rm BH} = (1.2 \pm 1.5) \times 10^8\,M_\odot$ for $0.04 < z < 0.85$, and $M_{\rm BH} = (7.4 \pm 6.4) \times 10^8\,M_\odot$ for $z > 0.85$. An Anderson–Darling test indicates the distributions of black hole masses at $z < 0.01$ and $0.01 < z < 0.04$ consistent with being drawn from the same population, but those at $0.04 < z < 0.85$ and $z > 0.85$ are drawn from the same population at less than the 1% level, consistent with their higher median black hole masses.

The higher median black hole masses found for high-redshift AGNs are likely a selection effect driven by the fixed survey flux limit.

The median and MAD values are $M_{\rm BH} = (1.9 \pm 2.6) \times 10^8\,M_\odot$ for Seyfert 1–1.9; $M_{\rm BH} = (1.9 \pm 2.1) \times 10^8\,M_\odot$ for Seyfert 2; $M_{\rm BH} = (1.7 \pm 2.1) \times 10^8\,M_\odot$ for LINERs; and $M_{\rm BH} = (6.0 \pm 6.0) \times 10^8\,M_\odot$ for beamed AGNs. An Anderson–Darling test indicates the distributions of black hole masses of Seyfert 1–1.9, Seyfert 2, and LINERS are consistent with being drawn from the same population, but the likelihood that beamed AGNs are drawn from the same population is less than the 1% level.

While we do not find any significant difference between the black hole mass distributions of Seyfert 1–1.9 and Seyfert 2, we note that our survey has systematic biases against the smaller black holes ($M_{\rm BH} < 10^7\,M_\odot$) in Seyfert 2 AGNs. Specifically, the velocity dispersion measurements for Seyfert 2 are limited by the instrumental broadening in lower spectral resolution setups. Typical instrumental resolutions are between 2 and 7 Å FWHM, (corresponding to limiting black hole masses of $M_{\rm BH} = 10^6$–$10^8\,M_\odot$). We have recently been granted two filler programs with VLT/XSHOOTER (K. Oh et al. 2017, in preparation) that will further address this issue, as the

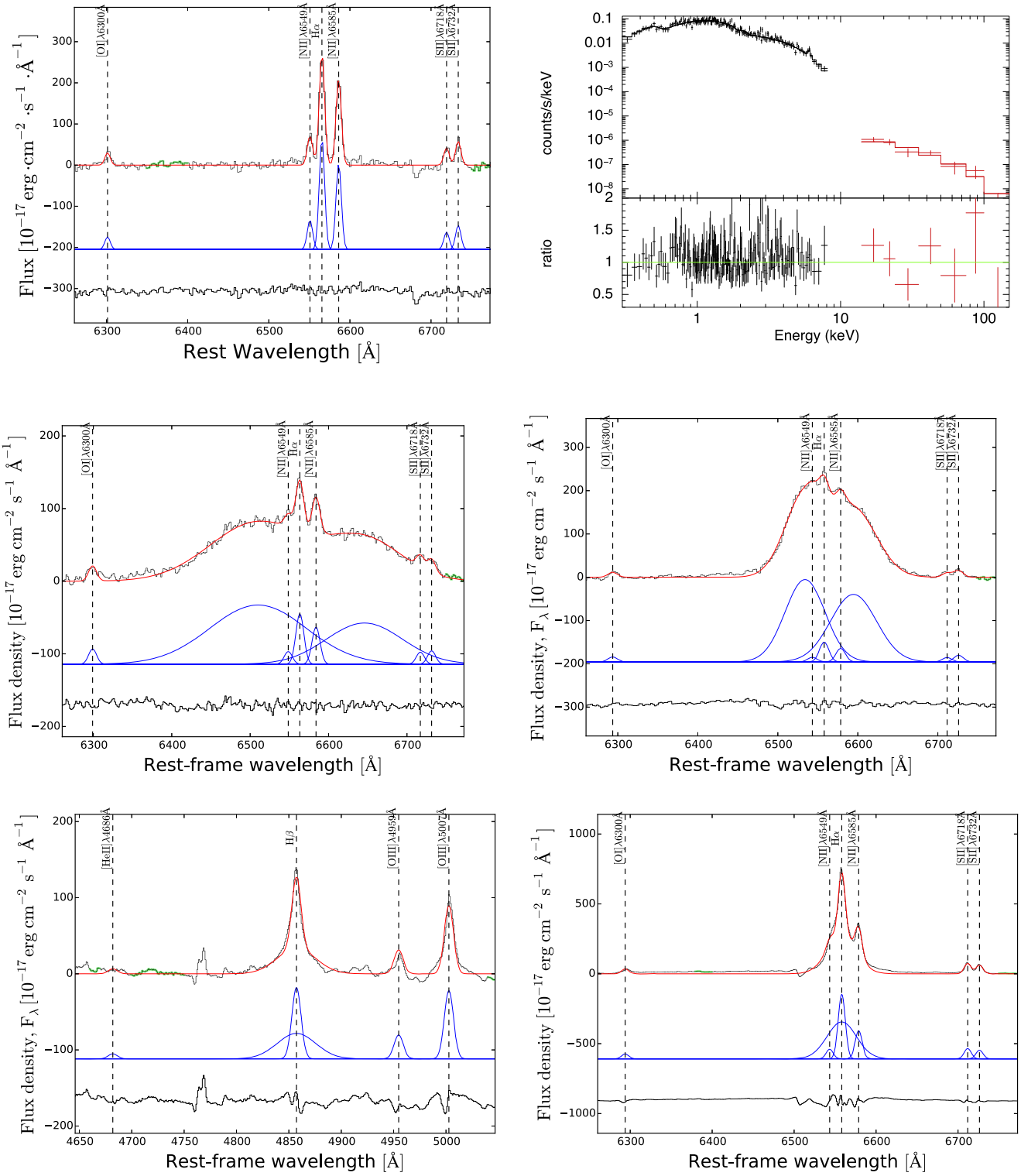

Figure 14. Examples of unusual AGNs. Top row: optical spectrum of "naked" candidate 2MASX J19263018+4133053 showing the Hα region (left) and *Swift*/XRT (red) and *Swift*-BAT (black) spectrum (right). We see no evidence of a broad Hα component in the optical and no evidence of obscuration in the X-rays. Middle row: optical spectrum of double-broad-line sources showing the Hα region of ESO 359-G 019 (left) and IGR J22292+6647 (right). The fit is composed of narrow Gaussian components added to two broad Hα components (in blue). The residual is shown below in gray. Bottom row: optical spectrum of the type 1 optically elusive Mrk 507 showing the Hβ region (left) and the Hα region (right). Both Hα and Hβ show a clear broad component, but weak narrow emission lines, characteristic of an H II region. The residual is shown below in gray.

spectral resolution would be sufficient to measure limiting black hole masses of $M_{\rm BH} = 10^5\,M_\odot$. A final issue is that for galaxies with a significant rotation component, σ_* measured from a single aperture spectrum can vary by up to ∼20%, depending on the size of the adopted extraction aperture (Kang et al. 2013).

We combined the M_{BH} estimates with the estimates of L_{bol}, derived from the BAT X-ray luminosity, to calculate the Eddington ratios of the BASS AGNs, L/L_{Edd} erg s^{-1}(where $L_{Edd} \equiv 1.3 \times 10^{38}\,(M_{BH}/M_{\odot})$). The maximum value of the bolometric luminosity of our sample is $L_{bol} = 10^{48.5}$ erg s^{-1}. The AGNs with higher L_{bol} have, in general, higher L/L_{Edd}, but there are also some AGNs with relatively high bolometric luminosity ($L_{bol} > 10^{45}$ erg s^{-1}) and low Eddington ratio ($L/L_{Edd} < 0.01$). The sources with the highest bolometric luminosity ($L_{bol} > 10^{47}$ erg s^{-1}), however, do have high accretion rates ($L/L_{Edd} > 0.1$). Conversely, several of the most massive BHs in unbeamed AGN in our sample ($M_{BH} > 10^{9.7}\,M_{\odot}$) also have the lowest accretion rates. Regarding the redshift distributions, the median and MAD Eddington ratios are $L/L_{Edd} = 0.005 \pm 0.008$ for $z < 0.01$, $L/L_{Edd} = 0.026 \pm 0.036$ for $0.01 < z < 0.04$, $L/L_{Edd} = 0.047 \pm 0.062$ for $0.04 < z < 0.85$, and $L/L_{Edd} = 1.46 \pm 2.16$ for $z > 0.85$. An Anderson–Darling test indicates each of the redshift distributions of Eddington ratios are each drawn from the same population at the less than 1% level, consistent with their steadily increasing medians. These properties of our sample are not surprising, given the flux limited (and low-redshift) nature of our sample.

Regarding the Eddington ratios among different Seyfert types, we do find that Seyfert 2 AGNs have, in general, lower Eddington ratios because Seyfert 1 AGNs have higher bolometric luminosities. The peak of the distribution for Seyfert 2 is at $L/L_{Edd} \simeq 0.01$. For the Seyfert 1 AGNs, the peak of the distribution is between $L/L_{Edd} = 0.01$ and 0.1, with a small number (13) of unbeamed sources above the Eddington limit, $L/L_{Edd} \gtrsim 1$. The median and MAD are $L/L_{Edd} = 0.10 \pm 0.09$ for Seyfert 1–1.9, $L/L_{Edd} = 0.014 \pm 0.014$ for Seyfert 2, and $L/L_{Edd} = 0.009 \pm 0.012$ for LINERs, and $L/L_{Edd} = 1.46 \pm 2.16$ for beamed AGNs.

We note that the Eddington ratios of beamed AGNs are derived from the observed luminosities (and masses), and have not been corrected for beaming angle. An Anderson–Darling test indicates that the distributions of Eddington ratios for Seyfert 2 AGNs and LINERs are consistent with being drawn from the same population. However, the likelihood that the Eddington ratios of type 1 and beamed AGNs are drawn from the same population is less than 1%, consistent with their much larger medians. It is interesting to note that using the observed Eddington ratios is highly efficient at separating beamed AGNs from unbeamed sources because typical beamed AGNs are above the Eddington limit.

We also found sources with extremely low accretion rates ($L/L_{Edd} < 0.001$). There are 15 type 2 AGNs and 13 type 1 AGNs with Eddington ratios $L/L_{Edd} < 0.001$. In general, type 1 AGNs are found to have high accretion rates, $L/L_{Edd} > 0.01$ (e.g., Nicastro 2000; Yuan & Narayan 2004; Trump et al. 2011; Elitzur et al. 2014), and therefore it is quite surprising to find type 1 sources with such a low value of the Eddington ratio.

4.6. Unusual AGNs

As we studied the properties of our sample in the optical and X-rays, a number of objects showed interesting and unusual characteristics. Some examples of these objects are presented in Figure 14. We discuss here four different types: AGNs with very low X-ray column density, but lacking broad emission lines, or vice versa; double-broad-line AGNs; and weak-line AGNs. We note that because the X-ray and optical spectroscopy are not simultaneous, the contradictory optical and X-ray classification could be caused by variability.

4.6.1. AGN with Contradictory Optical and X-Ray Classification

So-called "naked" AGN candidates (Hawkins 2004; Panessa et al. 2006) are objects showing an optical spectrum with no detectable broad emission lines in the optical (Seyfert 2) and no obscuration in the X-rays ($N_H < 10^{20.5}$ cm^{-2}). Therefore, they are intriguing because they contradict the basic expectation from the geometrical unification scheme of AGN. Six AGNs in our sample (≈1%) satisfy the "naked" AGN candidate criteria (2MASX J01302127–4601448, SDSS J155334.73+261441.4, LCRS B232242.2–384320, 2MASX J11271632+1909198, 2MASX J19263018+4133053, and PKS 2331-240): their optical spectra classify them as Seyfert 2, but we observe little obscuration in the X-rays ($N_H < 10^{20.5}$ cm^{-2}) with the 90% error bars below ($N_H < 10^{21}$ cm^{-2}).

Another interesting class of AGNs is objects that have broad Balmer emission lines (Seyfert 1, 1.2, and 1.5 AGN), but very high column densities of $N_H > 10^{23}$ cm^{-2} with $N_H > 10^{22.5}$ cm^{-2} for all 90% error bars. The five AGNs in our sample that satisfy these criteria are Mrk 975, CGCG 031-072, WISE J144850.99–400845.6, 3C 445, and 2MASXJ19301380+3410495. 3C 445 was already known to be a peculiar broad-line radio galaxy with an X-ray-absorbed spectrum that has multiple X-ray absorption components consistent with our findings (Grandi et al. 2007; Reeves et al. 2010). We note, however, that we do not find any Compton-thick Seyfert 1, 1.2, or 1.5, with the maximum column density of these sources never exceeding $N_H = 10^{23.7}$ cm^{-2}.

4.6.2. Double-broad-line AGNs

This sub-class of broad-line AGNs shows two broad and well-separated (in velocity space) Hα emission profiles. Previous studies have suggested several possible explanations for the origin of these double-broad-lines, including the relativistic accretion disk; a binary BLR in a binary BH system; bipolar outflows, or a spherically symmetric BLR illuminated by an anisotropic ionizing radiation source (see, e.g., Eracleous & Halpern 1994; Eracleous et al. 2009). A close visual inspection of our sample reveals only seven sources with such features (FBQS J110340.2, 2MASX J08032736, 3C 332, NGC 4235, MCG +09-21-096, 2MASX J21320220, ESO 359-G019).

4.6.3. Weak-line AGNs

The last category of peculiar objects that we consider are AGNs that lack some or all of the narrow-line emission typical of AGNs and cannot be studied using emission-line diagnostics. This category comprises 10% of the sample (65/642) using the [N II] λ6583/Hα emission-line diagnostic. Only three of the weak-line AGNs lack *any* detectable emission lines despite having high-quality spectra. These sources are consistent with X-ray bright optically normal galaxies (e.g., XBONGS, Comastri et al. 2002). The XBONGS are 2MASX J04595677+3502536, 2MASX J13553383+3520573, and ESO 436-G034. We have verified that the association of the BAT X-ray sources with other counterparts was not erroneous, by confirming that their soft X-ray counterparts are the

brightest counterparts in the field of view; that these AGNs are not associated with known (background) blazars or beamed AGNs; and that the optical spectra of these sources have high S/N in the continuum (S/N > 10). Our results are consistent with the idea that XBONGs are exceedingly rare (<0.5% at most) and confirms the idea that the large fractions found in distant X-ray surveys are likely caused by host galaxy dilution and the difficulty with detecting emission lines in dusty galaxies (e.g., Moran et al. 2002).

5. Summary, Conclusions, and Future Work

We present the first catalog and data release of the *Swift-BAT Spectroscopic Survey* ("BASS"). Starting from an all-sky catalog of AGNs detected in the 14–195 keV band, we analyze a total of 642 AGNs and host galaxies, using a compilation of optical spectra from public surveys and dedicated campaigns. This spectroscopic data set allows us to measure strong, narrow, and broad emission lines, and stellar velocity dispersions, and to derive estimates of black hole masses ($M_{\rm BH}$) and accretion rates ($L/L_{\rm Edd}$). Our main findings are as follows.

(i) There is a continuous increase in the fraction of broad-line (type 1) AGNs, both with broad Hβ and/or Hα, with increasing 14–195 keV and 2–10 keV X-ray luminosities. Also, the classification of obscured and unobscured sources based on the FWHM of the Balmer emission lines shows broad agreement with those based on the X-ray obscuration, with about 94% of AGNs being consistently classified, for the threshold set at $N_{\rm H} \simeq 10^{21.9}\,{\rm cm}^{-2}$. The sources classified as Seyfert 1.9 show a range of column densities, however.

(ii) Compared to narrow-line AGNs in the SDSS, the X-ray-selected AGNs in our sample that have emission lines include a much larger fraction of dustier galaxies (Hα/Hβ > 5). We find that the X-ray-selected AGNs show a relatively constant type 1 to type 2 fraction of about 60%, over a broad range of redshift, while the same fraction among SDSS AGNs is much lower and shows a strong dependence on redshift (2%–30%). The average [O III] λ5007 luminosity and velocity dispersion of BAT AGNs are higher than SDSS AGNs, consistent with their brighter X-ray emission, and the smaller number of BAT AGNs per sky area.

(iii) Using the [N II] λ6583/Hα emission-line diagnostic, about half (53%, 338/642) of the BAT AGNs are classified as Seyferts, with a few percent classified in each of the sub-classes of LINERs, composite galaxies, or H II regions. Another 15% reside in dusty galaxies, where the upper limits on Hβ imply either a Seyfert or LINER (10%, 61/642). Finally, about 20% reside in galaxies with weak or no emission lines or are associated with known blazars or beamed AGNs. The weaker lines involved in other diagnostics ([S II] λ6717,6731/Hα, [O I] λ6300/Hα, [O III] λ5007/[O II] λ3727, and He II/Hβ) have a lower detection fraction, but overall the sample is dominated by Seyfert AGNs.

(iv) We find that the accretion rates of Seyfert 1 AGNs (in terms of $L/L_{\rm Edd}$) are higher than those of Seyfert 2, mainly because Seyfert 1 AGNs have higher bolometric luminosities. With increasing redshift the survey tends to find higher $L/L_{\rm Edd}$ systems. Finally, using Eddington ratios is highly efficient at separating beamed AGNs from unbeamed sources because typical beamed AGNs are above the Eddington limit.

The present work provides a broad overview of the optical spectra of the BAT hard X-ray-selected AGNs (>10 keV). In future studies of this sample we will address in detail specific aspects of AGN physics and SMBH growth. Among the many follow-up opportunities, we note our recently published study of correlations between X-ray continuum emission and narrow-line emission (e.g., [O III]; Berney et al. 2015); a large study of the NIR spectra of over 100 BAT AGNs (Lamperti et al. 2017); and a study of trends in accretion rate with merger stage in interacting AGN hosts (M. Koss et al. 2017, in preparation). Another study investigates the role of accretion rate in emission-line ratios (Oh et al. 2017) and X-ray properties such as Γ (Trakhtenbrot et al. 2017), and obscuration (C. Ricci et al. 2017, in preparation). Finally, future optical spectroscopy studies will use deeper BAT maps that are now available to study fainter sources (K. Oh et al. 2017, in preparation). We therefore expect that the BASS sample will enable a wide variety of AGN studies in the local universe, and will serve as an important benchmark for high-redshift AGNs detected in deep, small-area surveys.

M.K. acknowledges support from the Swiss National Science Foundation (SNSF) through the Ambizione fellowship grant PZ00P2_154799/1 and SNSF grant PP00P2 138979/1, and K.O. and K.S. acknowledge support from the SNSF through Project grant 200021_157021. M.B. acknowledges support from NASA Headquarters under the NASA Earth and Space Science Fellowship Program, grant NNX14AQ07H. Support for the work of E.T. was provided by the Center of Excellence in Astrophysics and Associated Technologies (PFB 06), by the FONDECYT regular grant 1120061 and by the CONICYT Anillo project ACT1101. M.K. would like to thank Di Harmer at the NOAO for teaching him how to use the Goldcam spectrograph on his first optical spectroscopy run.

This paper used archival optical spectroscopic data from several telescopes. Kitt Peak National Observatory, National Optical Astronomy Observatory, is operated by the Association of Universities for Research in Astronomy (AURA), Inc., under cooperative agreement with the National Science Foundation. The Kitt Peak National Observatory observations were obtained using MD-TAC time as part of the thesis of M. K. (2008A-0393,2009B-0295) and L.W. at the University of Maryland. We also acknowledge the following people who assisted in the Palomar observations presented herein: Kristen Boydstun, Clarke Esmerian, Carla Fuentes, David Girou, Ana Glidden, Hyunsung Jun, George Lansbury, Ting-Ni Lu, Alejandra Melo, Eric Mukherjee, Becky Tang, and Dominika Wylezalek. This paper uses observations made at the South African Astronomical Observatory (SAAO).

Data in this paper were acquired through the Gemini Science Archive and processed using the Gemini IRAF package and Gemini python. Data from Gemini programs GN-2009B-Q-114, GN-2010A-Q-35, GN-2011A-Q-81, GN-2011B-Q-96, GN-2012A-Q-28, GN-2012B-Q-25, GS-2010A-Q-54, and GS-2011B-Q80 were used in this publication and included NOAO-granted community-access time for 2011B-0559 (PI Koss). This work is based on observations obtained at the Gemini Observatory and processed using the Gemini IRAF

package, which is operated by the Association of Universities for Research in Astronomy, Inc., under a cooperative agreement with the NSF on behalf of the Gemini partnership: the National Science Foundation (United States), the National Research Council (Canada), CONICYT (Chile), Ministerio de Ciencia, Tecnología e Innovación Productiva (Argentina), and Ministério da Ciência, Tecnologia e Inovação (Brazil). The authors wish to recognize and acknowledge the very significant cultural role and reverence that the summit of Maunakea has always had within the indigenous Hawaiian community. We acknowledge the efforts of the staff of the Australian Astronomical Observatory (AAO), who developed the 6dF instrument and carried out the observations for the survey. We are most fortunate to have the opportunity to conduct observations from this mountain.

Funding for SDSS-III has been provided by the Alfred P. Sloan Foundation, the Participating Institutions, the National Science Foundation, and the U.S. Department of Energy Office of Science. The SDSS-III web site is http://www.sdss3.org/. SDSS-III is managed by the Astrophysical Research Consortium for the Participating Institutions of the SDSS-III Collaboration including the University of Arizona, the Brazilian Participation Group, Brookhaven National Laboratory, University of Cambridge, Carnegie Mellon University, University of Florida, the French Participation Group, the German Participation Group, Harvard University, the Instituto de Astrofisica de Canarias, the Michigan State/Notre Dame/JINA Participation Group, Johns Hopkins University, Lawrence Berkeley National Laboratory, Max Planck Institute for Astrophysics, Max Planck Institute for Extraterrestrial Physics, New Mexico State University, New York University, The Ohio State University, Pennsylvania State University, University of Portsmouth, Princeton University, the Spanish Participation Group, University of Tokyo, University of Utah, Vanderbilt University, University of Virginia, University of Washington, and Yale University.

Finally, we wish to acknowledge several community software resources and websites. IRAF is distributed by the National Optical Astronomy Observatory, which is operated by the Association of Universities for Research in Astronomy (AURA) under a cooperative agreement with the National Science Foundation. This research has made use of the NASA/IPAC Extragalactic Database (NED) which is operated by the Jet Propulsion Laboratory, California Institute of Technology, under contract with the National Aeronautics and Space Administration. This research made use of Astropy, a community-developed core Python package for Astronomy (Robitaille et al. 2013). This research made use of APLpy, an open-source plotting package for Python hosted at http://aplpy.github.com. This research has made use of the SIMBAD database, operated at CDS, Strasbourg, France.

Facilities: Swift, UH:2.2m, Sloan, KPNO:2.1m, FLWO:1.5m (FAST), Shane (Kast Double spectrograph), CTIO:1.5m, Hale, Gemini:South, Gemini:Gillett, Radcliffe, Perkins.

Appendix A

We performed a variety of checks on our galaxy template fitting, velocity dispersion, emission-line-fitting, black hole mass, and bolometric luminosity measurements, and we describe them here.

A.1. Galaxy Template Fitting and Velocity Dispersion Measurements

Examples of the velocity dispersion fits from different telescopes can be found in Figures 15 and 16. We first compared our results for the spectra from SDSS with the values given from the SDSS 12th data release, measured using a direct fitting method rather than pPXF (Figure 17). The values calculated using pPXF are in good agreement, with maximal differences always less than 50 km s^{-1}.

We also compared velocity dispersion σ_*, using pPXF, to literature values obtained with other telescopes. We used the data from the Hyperleda catalog (Paturel et al. 2003) and literature references (Cid Fernandes et al. 2004; Garcia-Rissmann et al. 2005; Ho et al. 2009; van den Bosch et al. 2015). For 41 galaxies in our sample we found a value of σ_* in the literature. Figure 18 shows the comparison plot. Most (31/41, 76%) of the obtained values are in agreement with the literature values, with the differences between our values and the literature at $<$50 km s^{-1}. For 10/41 (24%) of sources, the difference is between 50 and 100 km s^{-1} and none are above this value.

We used Monte Carlo (MC) simulations to check the velocity dispersion σ_* measured by pPxf and any possible systematics with larger noise. We considered five spectra from different telescopes (SDSS, KPNO, 6dF) with different values for the pPXFerrors (10, 20, 30 km s^{-1}). Then, we added random noise to the spectrum to increase the values of the pPXFerror until an established level (20, 30, 40, 50 km s^{-1}). For every level of noise, we ran 100 MC simulations and we calculated the mean of the results obtained for σ_*. The difference between the original value $\sigma_{*,\mathrm{ppxf}}$ and the mean value from the MC simulations $\sigma_{*,\mathrm{MC}}$ is always smaller than 20 km s^{-1} (Figure 19).

A.2. Emission-line Measurements

We provide several examples of our emission-line fits using different telescopes. A separate BASS study found that the physical slit size, telescope sample, or X-ray obscuration level was not a significant contributor to the scatter in emission-line measurements compared to the X-ray emission (Berney et al. 2015) for sources with $0.01 < z < 0.4$, where the size of the slit is typically kiloparsec scales. With some setups we were able to cover the blue [Ne V] λ3426, [O II] λ3727, and [Ne III] λ3968 region (e.g., Figure 20) in addition to the Hβ and Hα regions (e.g., Figure 21). We tested our emission-line measurements with a number of literature values to confirm their accuracy. Figure 22 shows the comparison between values from the OSSY catalog (Oh et al. 2011) and our measured values for the [O III] emission-line flux derived from the same SDSS spectra. We obtain a standard deviation of $\sigma = 0.051$ dex and a median offset of 0.014 dex for flux values over three orders of magnitude.

We also tested how the inclusion of the effect of fitting empirical models with absorption lines that we applied to all narrow-line sources changes the emission-line measurements. Due to the absorption features on Hα and Hβ, the obtained values for the two Balmer lines are often underevaluated. The effect is more pronounced for the Hβ emission line. The result on the line diagnostic diagram is a strong shift to the bottom of the diagram and a relatively small shift to the left, which is toward the H II and Composite regions (See Figure 23). We note that in this study this fitting correction for absorption has only

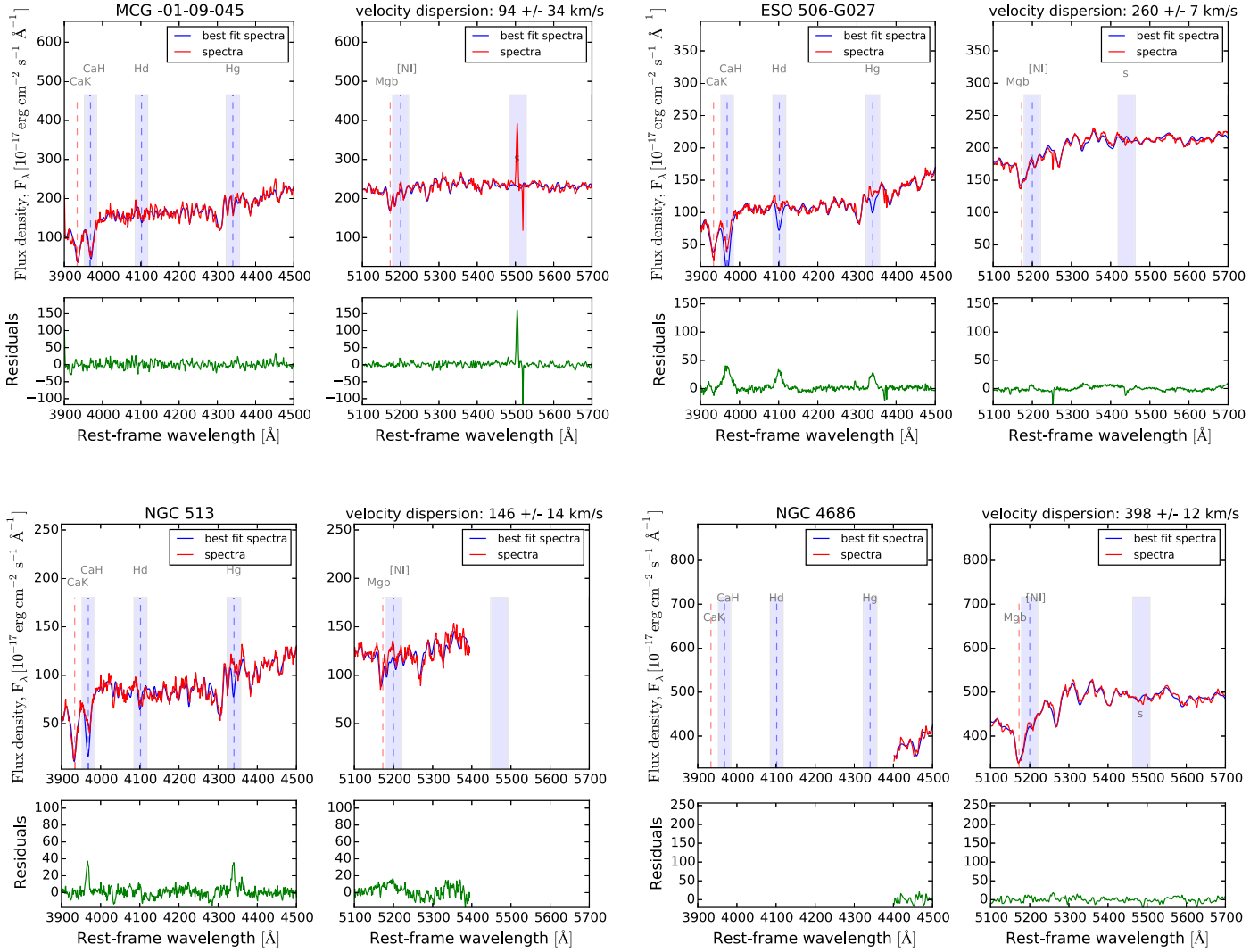

Figure 15. Example PPXFfits for the galaxies MCG-01-09-045 (upper left) taken with UK Schmidt, ESO 506-G027 (upper right) taken with Gemini, NGC 513 (bottom left) taken with CTIO 1.5 m, and NGC 4686 (bottom right) taken with Kitt Peak 2.1 m. The green bottom portion shows the residuals that include the masked emission lines. The fits of these galaxies have flag 1, meaning that the residuals are small and the error in the value of the velocity dispersion is small. The blue regions are the wavelength regions that we mask in order to exclude the contamination on the stellar continuum due to emission lines and sky features. For NGC 4686, we fit only from 4400 Å because the wavelength range of this spectrum does not cover the CaH+K region.

been done for narrow-line sources, where the empirical model fits are not biased by AGN light.

A.3. Black Hole Mass

We compared our black hole mass measurements (Figure 24) using broad-line measurements of the Hβ or Hα regions in single-epoch observations. We also compare the mass measurements to higher-quality reverberation mapping measurements for the small sample where these are available. We find that the slope is consistent with unity, with fairly large scatter (≈0.4–0.5 dex).

We also made a comparison of Seyfert 1.9 black hole masses, measured with very weak broad Hα lines, to those with no broad Hβ detected (Figure 25). We find that below equivalent widths (EWs) of 50 Å in Hα, the velocity dispersion differs significantly, suggesting these broad features could be spurious; thus we have used this limit for flag 2 sources in our sample. The value of this limit is consistent with many past quasar studies (e.g., EW $<$ 45 Å; Shen et al. 2011), though some studies of nearby AGNs have used much weaker broad lines (e.g., EW $<$ 15 Å; Greene & Ho 2007).

The offset in black hole mass measurements between Seyfert 1.9 using velocity dispersion measurements and broad-line Hα is concerning, though offsets have been found in AGN samples (e.g., Shankar et al. 2017). We note, however, that these two methods are tied to reproduce similar masses for systems where both are applicable (e.g., Graham et al. 2011; Woo et al. 2013), so it is likely that the subsample of Seyfert 1.9 explored here is not representative. One particular concern is that the weak broad-line Hα may suffer high extinction and is underestimated, which we are exploring in a current VLT/XSHOOTER program using the NIR broad Paschen emission lines (K. Oh et al. 2017, in preparation).

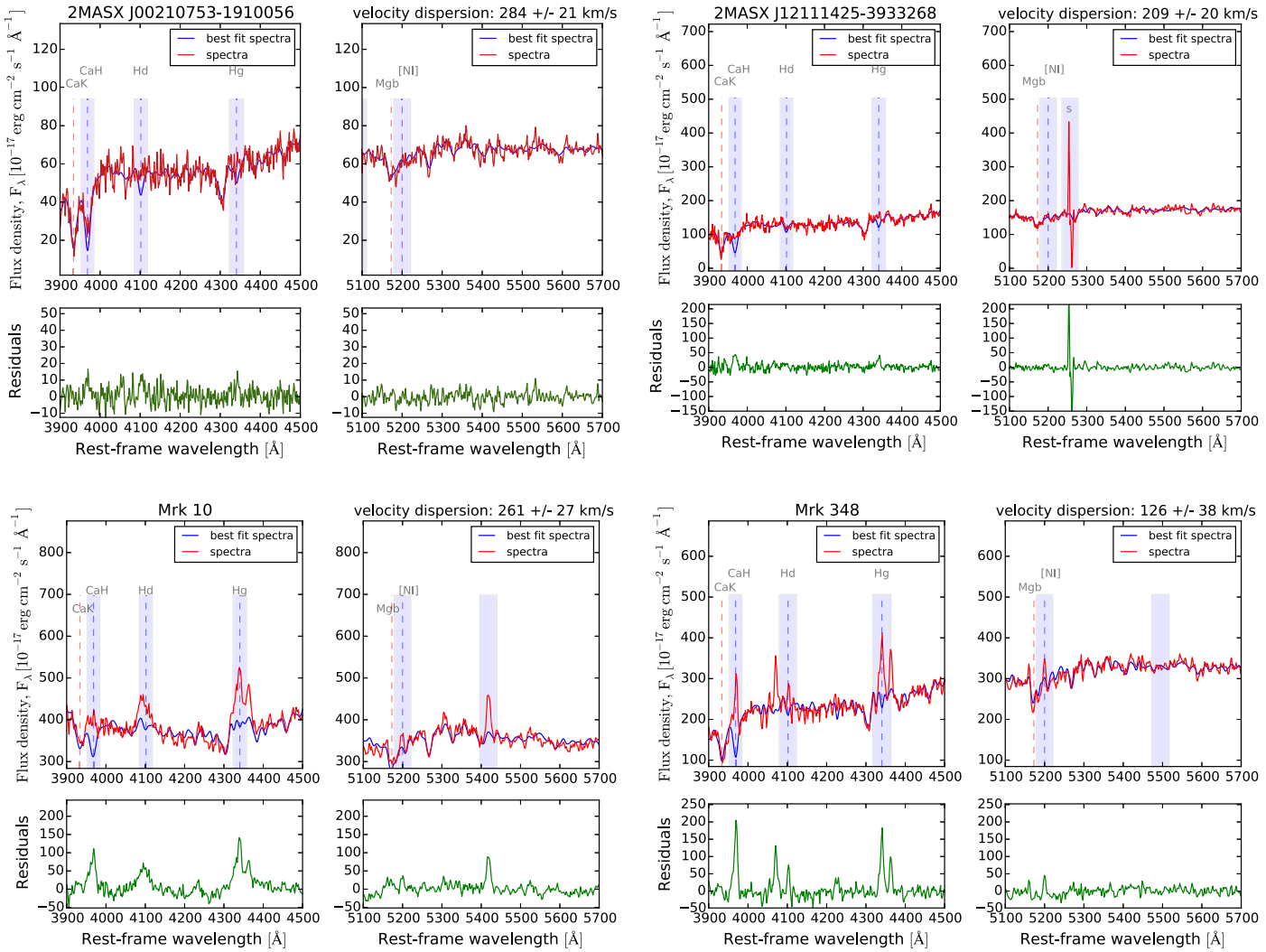

Figure 16. Example PPXFfits for the galaxies 2MASX J00210753–1910056 (upper left) taken with UK Schmidt, 2MASX J12111425–3933268 (upper right) taken with UK Schmidt, Mrk 10 (bottom left) taken with CTIO 1.5 m, and Mrk 348 (bottom right) taken with CTIO 1.5 m. The fits of these galaxies have flag 2, meaning that the fit of the stellar continuum is not very precise, but the absorption lines of Ca H+K and Mg I are well fitted and the value of the velocity dispersion is sufficiently precise to rely on it. The blue regions are the wavelength regions that we mask in order to exclude the contamination on the stellar continuum due to emission lines and sky features.

A.4. Bolometric Luminosity

For consistency, we compare our values of the bolometric luminosity $L_{\rm bol}$, derived from the X-ray luminosity, with the values of $L_{\rm bol}$ obtained from the optical luminosity at 5100 Å (e.g., Wandel et al. 1999) for Seyfert 1 AGNs. In Figure 26, comparisons between the $L_{\rm bol}$ obtained from the X-ray bolometric corrections and the $L_{\rm bol}$ derived from the optical luminosity are shown. The two methods to infer $L_{\rm bol}$ show fairly larger scatter (0.46 dex), with more scatter at high luminosities.

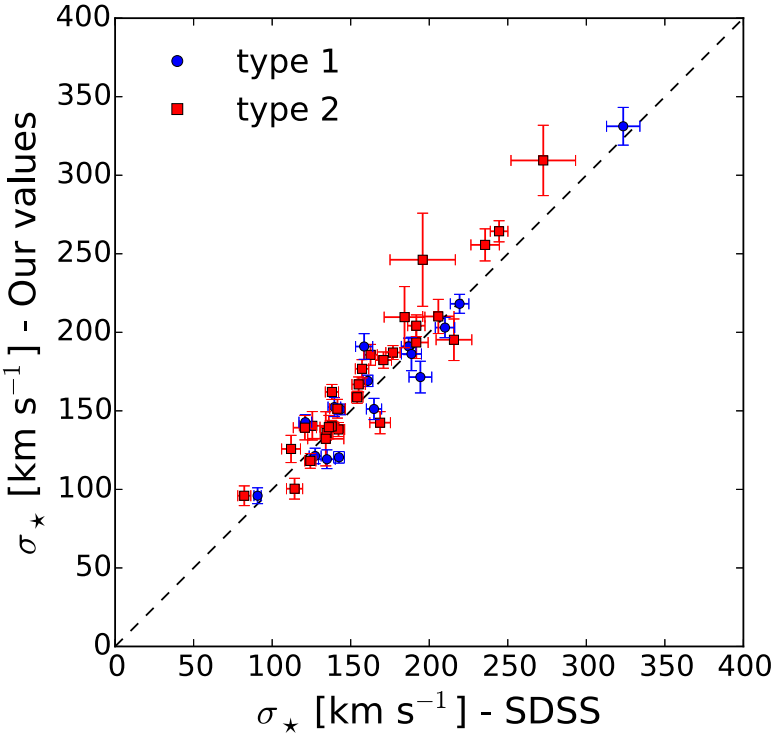

Figure 17. Comparison plot between the values of the velocity dispersion from the SDSS 12th data release, measured with a direct fitting method and our values obtained using PPXF.

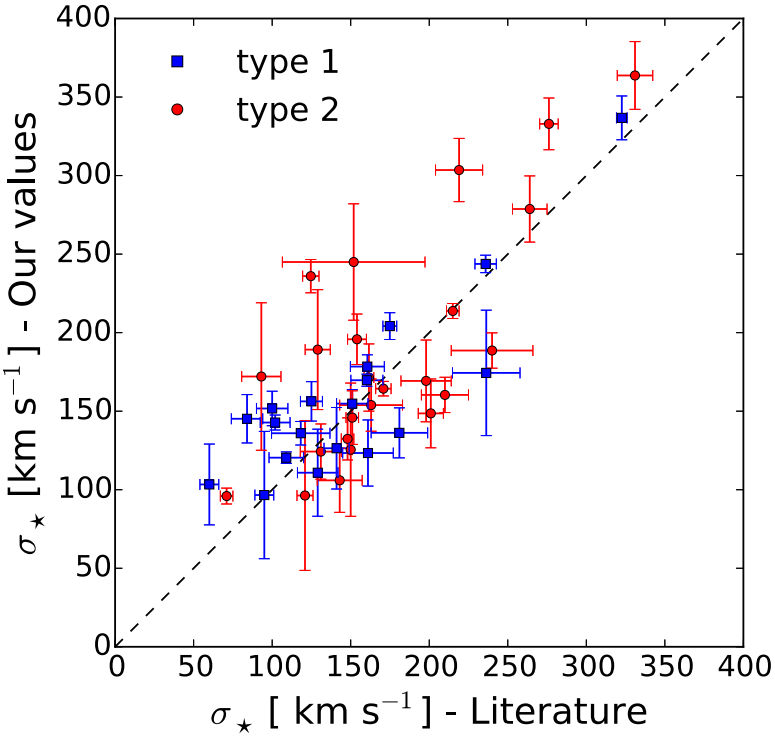

Figure 18. Comparison plot between the values of the velocity dispersion from the literature and those from our values obtained using PPXF.

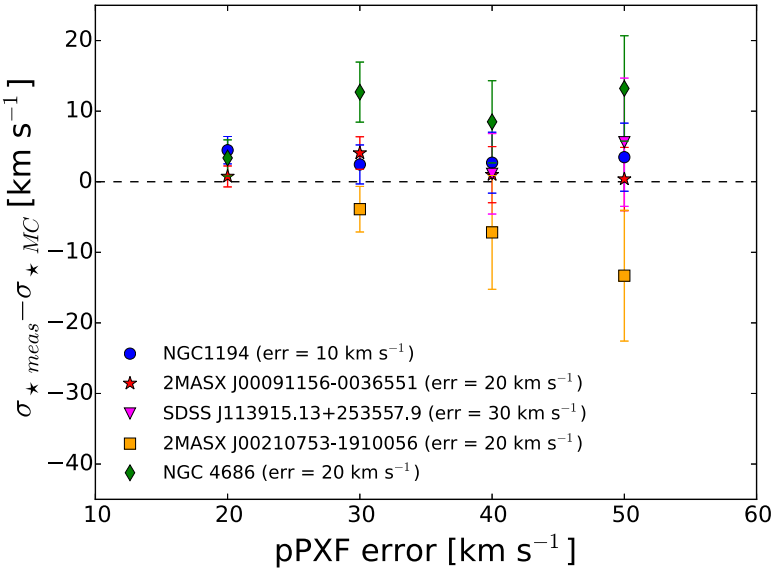

Figure 19. Difference between the value of the velocity dispersion measured by PPXF $\sigma_{*,\mathrm{meas}}$ and the mean value obtained from the MC simulations $\sigma_{*,\mathrm{MC}}$ as a function of the level of the error on σ_* measured by PPXF for five different spectra. The spectra are taken from SDSS, KPNO, and 6dF. The values of the error on σ_* measured by PPXF (before adding noise) for each spectrum are listed in brackets in the legend.

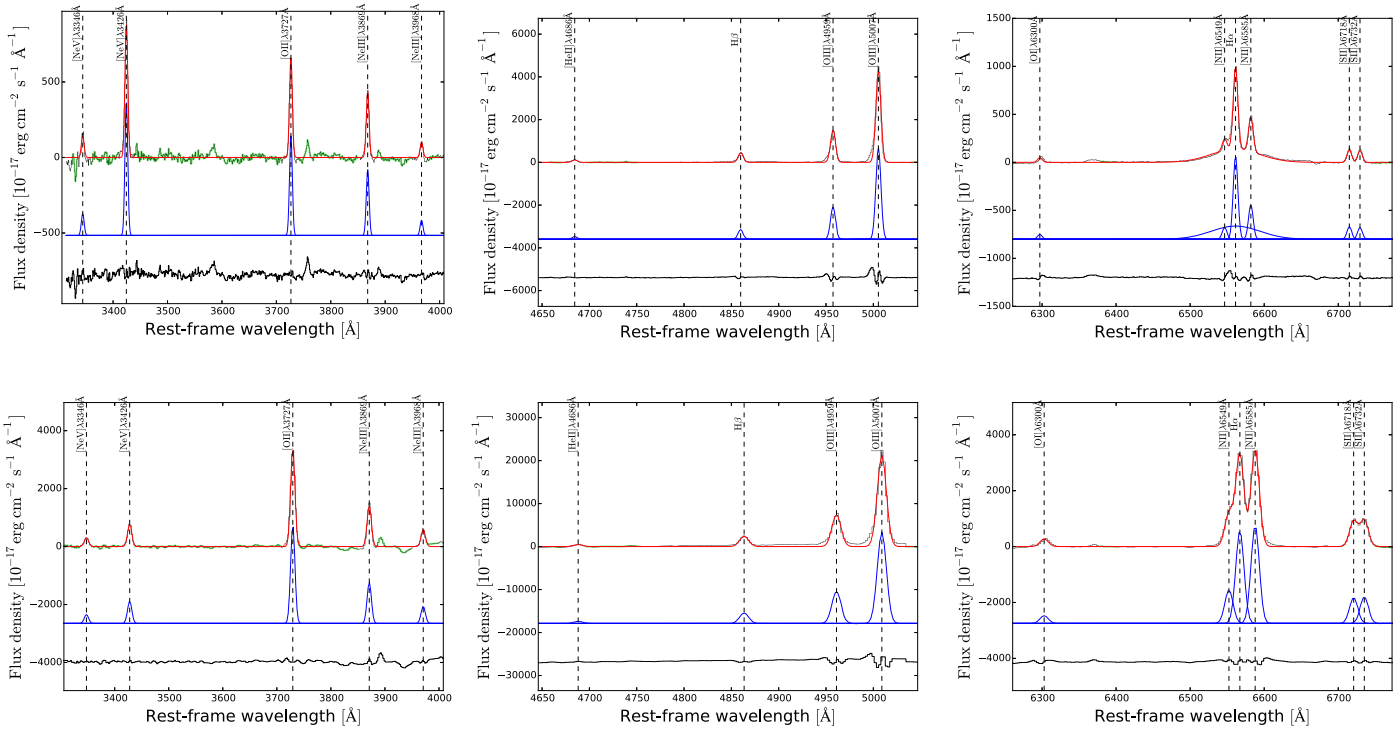

Figure 20. Example of emission-line fits for the galaxies CGCG 164-019 (upper row) taken with Palomar and NGC 3393 (lower row) taken with UH 2.2 m. The left panels show the fits of the blue [Ne V] λ3426, [O II] λ3727, and [Ne III] λ3968 region, the middle panels show the fits of the Hβ region, and the right panels show the fits of the Hα region.

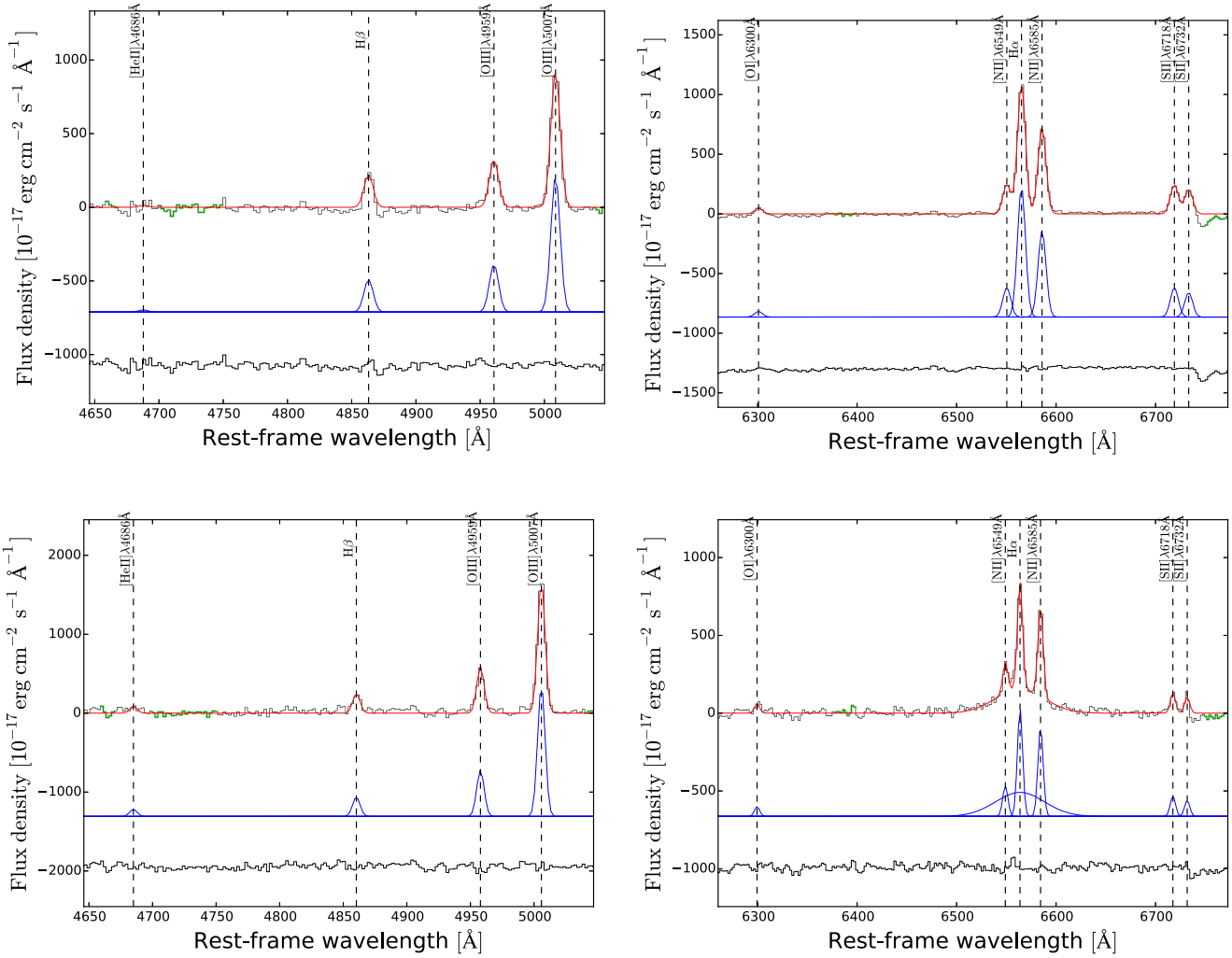

Figure 21. Example of emission-line fits for galaxy 2MASX J03534246+3714077 (upper row) taken with KPNO and 2MASX J05353211+4011152 (lower row) taken with the Perkins 1.8 m. The left panels show the fits of the Hβ region, and the right panels show the fits of the Hα region.

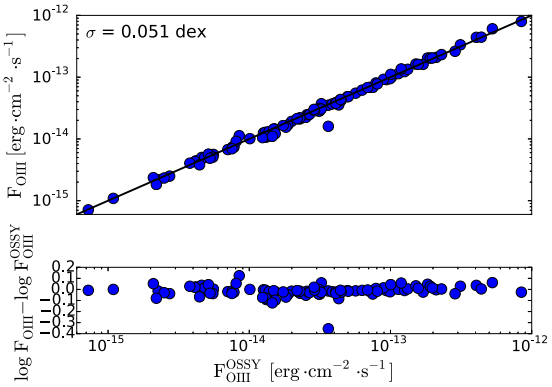

Figure 22. Log–log plot of the [O III] λ5007 flux values from 96 objects in the OSSY catalog (Oh et al. 2011) on the x-axis, and our measured values on the y-axis. The standard deviation and the median of the offset are written in the top left corner. The bottom panel shows the offset in log space between the OSSY values and our values.

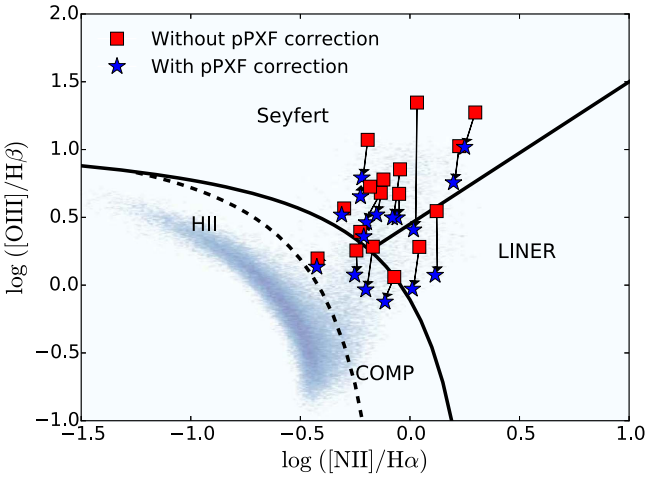

Figure 23. Effect of stellar absorption on the line diagnostic classification (Kewley et al. 2006) for 16 objects. The red squares show the classification without PPXF absorption line-fitting, and the blue stars show the classification after the absorption line-fitting. The arrows represent the movement of each point on the diagram. The gray area represents the SDSS sample (SNR $>$ 2.5 for lines). The solid line that separates Seyferts from LINERs is from Schawinski et al. (2007a).

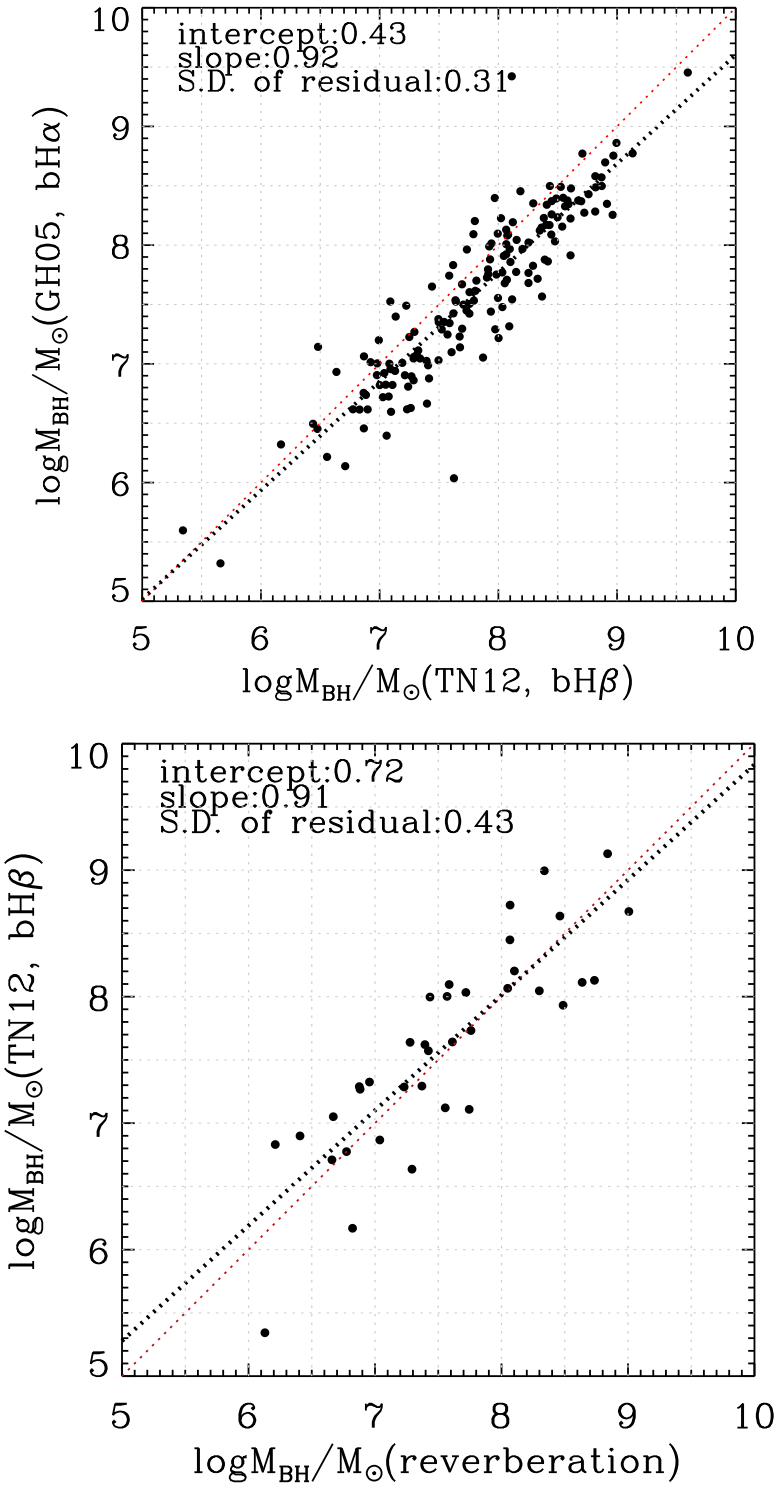

Figure 24. Top: comparison of black hole masses from broad Hβ (Trakhtenbrot & Netzer 2012) and broad Hα (Greene & Ho 2005b). Bottom: comparison of single-epoch broad Hβ measurements to reverberation mapping (Bentz & Katz 2015). A one-to-one fiducial line and linear regression fit are shown with red and black dotted lines, respectively, for both figures.

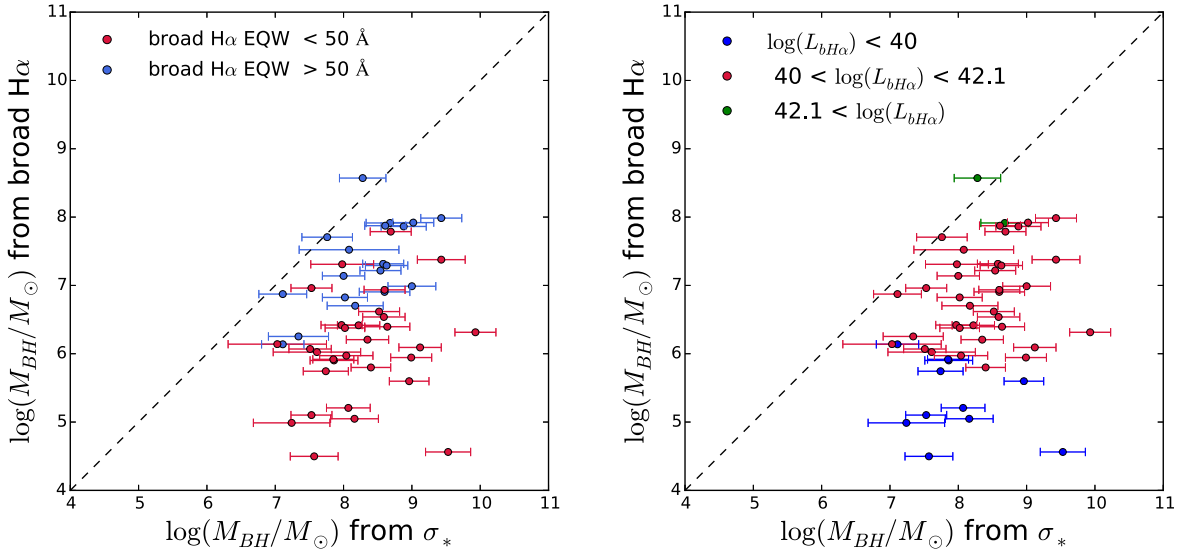

Figure 25. Comparison of black hole masses for Seyfert 1.9 galaxies derived from the velocity dispersion and from the broad Hα. We find that at low EWs (<50 Å), there is a significant difference between measurements of σ_* and broad Hα.

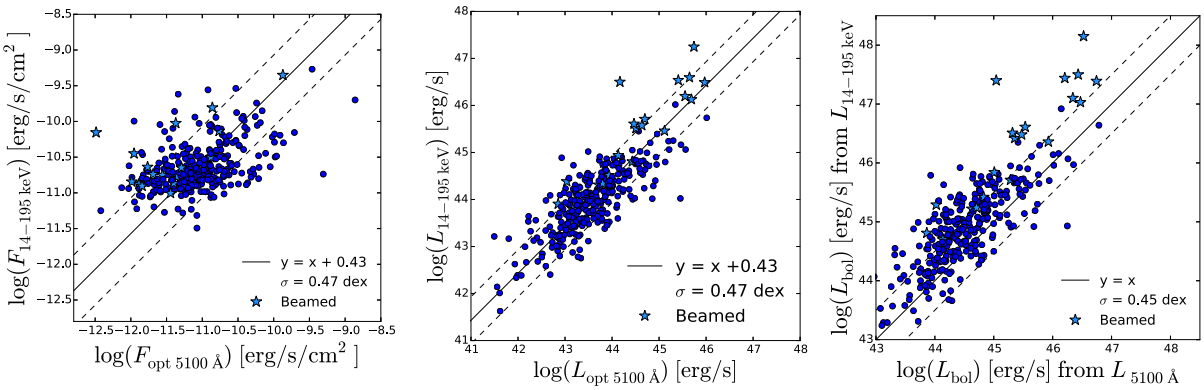

Figure 26. Relation between the X-ray emission and optical 5100 Å emission shown in flux (left panel) and luminosity (middle panel). The right panel shows the comparison between the bolometric luminosity derived from the X-ray luminosity and the bolometric luminosity derived from the optical luminosity for broad-line Seyfert 1 galaxies.

ORCID iDs

Michael Koss https://orcid.org/0000-0002-7998-9581
Benny Trakhtenbrot https://orcid.org/0000-0002-3683-7297
Claudio Ricci https://orcid.org/0000-0001-5231-2645
Isabella Lamperti https://orcid.org/0000-0003-3336-5498
Kyuseok Oh https://orcid.org/0000-0002-5037-951X
Kevin Schawinski https://orcid.org/0000-0001-5464-0888
D. Michael Crenshaw https://orcid.org/0000-0002-6465-3639
Travis Fischer https://orcid.org/0000-0002-3365-8875
Fiona Harrison https://orcid.org/0000-0003-2992-8024
Kohei Ichikawa https://orcid.org/0000-0002-4377-903X
Nicola Masetti https://orcid.org/0000-0001-9487-7740
Richard Mushotzky https://orcid.org/0000-0002-7962-5446
Daniel Stern https://orcid.org/0000-0003-2686-9241
Yoshihiro Ueda https://orcid.org/0000-0001-7821-6715
Sylvain Veilleux https://orcid.org/0000-0002-3158-6820
Lisa Winter https://orcid.org/0000-0002-3983-020X

References

Acker, A., Köppen, J., Samland, M., & Stenholm, B. 1989, Msngr, 58, 44
Alam, S., Albareti, F. D., Allende Prieto, C., et al. 2015, ApJS, 219, 12
Aldering, G., Antilogus, P., Bailey, S., et al. 2006, ApJ, 650, 510
Bacon, R., Copin, Y., Monnet, G., et al. 2001, MNRAS, 326, 23
Baldwin, J. A., Phillips, M. M., & Terlevich, R. 1981, PASP, 93, 5
Baloković, M., Comastri, A., Harrison, F. A., et al. 2014, ApJ, 794, 111
Bauer, F. E., Condon, J. J., Thuan, T. X., & Broderick, J. J. 2000, ApJS, 129, 547
Baumgartner, W. H., Tueller, J., Markwardt, C. B., et al. 2013, ApJS, 207, 19
Bentz, M. C., & Katz, S. 2015, PASP, 127, 67
Bentz, M. C., Peterson, B. M., Pogge, R. W., Vestergaard, M., & Onken, C. A. 2006, ApJ, 644, 133
Bentz, M. C., Walsh, J. L., Barth, A. J., et al. 2009, ApJ, 705, 199
Berney, S., Koss, M., Trakhtenbrot, B., et al. 2015, MNRAS, 454, 3622
Boroson, T. A., & Green, R. F. 1992, ApJS, 80, 109
Brandt, W. N., & Alexander, D. M. 2015, A&ARv, 23, 1
Brightman, M., Baloković, M., Stern, D., et al. 2015, ApJ, 805, 41
Capetti, A., Marconi, A., Macchetto, D., & Axon, D. 2005, A&A, 431, 465
Cappellari, M., & Emsellem, E. 2004, PASJ, 116, 138
Cappellari, M., Neumayer, N., Reunanen, J., et al. 2009, MNRAS, 394, 660
Cardelli, J. A., Clayton, G. C., & Mathis, J. S. 1989, ApJ, 345, 245
Cid Fernandes, R., Gu, Q., Melnick, J., et al. 2004, MNRAS, 355, 273

Civano, F., Marchesi, S., Comastri, A., et al. 2016, ApJ, 819, 62
Comastri, A., Mignoli, M., Ciliegi, P., et al. 2002, ApJ, 571, 771
Comastri, A., Setti, G., Zamorani, G., & Hasinger, G. 1995, A&A, 296, 1
Denney, K. D. 2012, ApJ, 759, 44
Devereux, N., Ford, H., Tsvetanov, Z., & Jacoby, G. 2003, AJ, 125, 1226
Draper, A. R., & Ballantyne, D. R. 2010, ApJL, 715, L99
Elitzur, M., Ho, L. C., & Trump, J. R. 2014, MNRAS, 438, 3340
Eracleous, M., & Halpern, J. P. 1994, ApJS, 90, 1
Eracleous, M., Lewis, K. T., & Flohic, H. M. L. G. 2009, NewAR, 53, 133
Ferrarese, L., & Merritt, D. 2000, ApJL, 539, L9
Garcia-Rissmann, A., Vega, L. R., Asari, N. V., et al. 2005, MNRAS, 359, 765
Ginsburg, A., & Mirocha, J. 2011, PySpecKit: Python Spectroscopic Toolkit, Astrophysics Source Code Library, ascl:1109.001
Graham, A. W., Onken, C. A., Athanassoula, E., & Combes, F. 2011, MNRAS, 412, 2211
Grandi, P., Guainazzi, M., Cappi, M., & Ponti, G. 2007, MNRAS, 381, L21
Greene, J. E., & Ho, L. C. 2005a, ApJ, 627, 721
Greene, J. E., & Ho, L. C. 2005b, ApJ, 630, 122
Greene, J. E., & Ho, L. C. 2007, ApJ, 667, 131
Grier, C. J., Martini, P., Watson, L. C., et al. 2013, ApJ, 773, 90
Guainazzi, M., Dennefeld, M., Piro, L., et al. 2000, A&A, 355, 113
Gültekin, K., Richstone, D. O., Gebhardt, K., et al. 2009, ApJ, 698, 198
Hawkins, M. R. S. 2004, A&A, 424, 519
Herrnstein, J. R., Moran, J. M., Greenhill, L. J., & Trotter, A. S. 2005, ApJ, 629, 719
Ho, L. C., Greene, J. E., Filippenko, A. V., & Sargent, W. L. W. 2009, ApJS, 183, 1
Jones, D. H., Read, M. A., Saunders, W., et al. 2009, MNRAS, 399, 683
Jones, D. H., Saunders, W., Colless, M., et al. 2004, MNRAS, 355, 747
Kang, W.-R., Woo, J.-H., Schulze, A., et al. 2013, ApJ, 767, 26
Kaspi, S., Smith, P. S., Netzer, H., et al. 2000, ApJ, 533, 631
Kewley, L. J., Groves, B., Kauffmann, G., & Heckman, T. 2006, MNRAS, 372, 961
Kewley, L. J., Heisler, C. A., Dopita, M. A., & Lumsden, S. 2001, ApJS, 132, 37
Kondratko, P. T., Greenhill, L. J., & Moran, J. M. 2005, ApJ, 618, 618
Kondratko, P. T., Greenhill, L. J., & Moran, J. M. 2008, ApJ, 678, 87
Kormendy, J., & Ho, L. C. 2013, ARA&A, 51, 511
Koss, M., Mushotzky, R., Treister, E., et al. 2012, ApJL, 746, L22
Koss, M. J., Assef, R., Baloković, M., et al. 2016a, ApJ, 825, 85
Koss, M. J., Glidden, A., Baloković, M, et al. 2016b, ApJL, 824, L4
Koss, M. J., Romero-Canizales, C., Baronchelli, L., et al. 2015, ApJ, 807, 149
Kuo, C. Y., Braatz, J. A., Condon, J. J., et al. 2011, ApJ, 727, 20
Lamassa, S., Urry, C. M., Cappelluti, N., et al. 2016, ApJ, 817, 172
Lamperti, I., Koss, M., Trakhtenbrot, B., et al. 2017, MNRAS, 467, 540
Landi, R., Masetti, N., Morelli, L., et al. 2007, ApJ, 669, 109
Landt, H., Bentz, M. C., Ward, M. J., et al. 2008, ApJS, 174, 282
Levine, A. M., Lang, F. L., Lewin, W. H. G., et al. 1984, ApJS, 54, 581
Lodato, G., & Bertin, G. 2003, A&A, 398, 517
Mahony, E. K., Sadler, E. M., Croom, S. M., et al. 2011, MNRAS, 417, 2651
Malizia, A., Landi, R., Molina, M., et al. 2016, MNRAS, 460, 19
Marchesi, S., Civano, F., Elvis, M., et al. 2016, ApJ, 817, 34
Marconi, A., Risaliti, G., Gilli, R., et al. 2004, MNRAS, 351, 169
Markwardt, C. B., Tueller, J., Skinner, G. K., et al. 2005, ApJL, 633, L77
Marziani, P., Sulentic, J. W., Zamanov, R., et al. 2003, ApJS, 145, 199
Masetti, N., Palazzi, E., Bassani, L., Malizia, A., & Stephen, J. B. 2004, A&A, 426, L41
Masetti, N., Bassani, L., Bazzano, A., et al. 2006a, A&A, 448, 547
Masetti, N., Mason, E., Bassani, L., et al. 2006c, A&A, 455, 11
Masetti, N., Mason, E., Morelli, L., et al. 2008, A&A, 482, 113
Masetti, N., Morelli, L., Palazzi, E., et al. 2006b, A&A, 449, 1139
Masetti, N., Parisi, P., Jiménz-Bailón, E., et al. 2012, A&A, 538, A123
Masetti, N., Parisi, P., Palazzi, E., et al. 2010, A&A, 519, A96
Masetti, N., Parisi, P., Palazzi, E., et al. 2013, A&A, 556, A120
Masetti, N., Pretorius, M. L., Palazzi, E., et al. 2006d, A&A, 459, 21
Massaro, E., Giommi, P., Leto, C., et al. 2009, A&A, 495, 691
McConnell, N. J., & Ma, C.-P. 2013, ApJ, 764, 184
Medling, A. M., Ammons, S. M., Max, C. E., et al. 2011, ApJ, 743, 32
Merloni, A., Bongiorno, A., Brusa, M., et al. 2014, MNRAS, 437, 3550
Merritt, D. 1997, AJ, 114, 228
Mor, R., Netzer, H., & Elitzur, M. 2009, ApJ, 705, 298
Moran, E. C., Filippenko, A. V., & Chornock, R. 2002, ApJL, 579, L71
Nelson, C. H., Green, R. F., Bower, G., Gebhardt, K., & Weistrop, D. 2004, ApJ, 615, 652
Nelson, C. H., & Whittle, M. 1995, ApJS, 99, 67
Nicastro, F. 2000, ApJL, 530, L65
Oh, K., Sarzi, M., Schawinski, K., & Yi, S. K. 2011, ApJS, 195, 13
Oh, K., Schawinski, K., Koss, M., et al. 2017, MNRAS, 464, 1466
Oh, K., Yi, S. K., Schawinski, K., et al. 2015, ApJS, 219, 1
Onken, C. A., Valluri, M., Brown, J. S., et al. 2014, ApJ, 791, 37
Osterbrock, D. E. 1981, ApJ, 249, 462
Osterbrock, D. E., & Pogge, R. W. 1985, ApJ, 297, 166
Panessa, F., Bassani, L., Cappi, M., et al. 2006, A&A, 455, 173
Parisi, P., Masetti, N., Jiménz-Bailón, E., et al. 2009, A&A, 507, 1345
Parisi, P., Masetti, N., Jiménz-Bailón, E., et al. 2012, A&A, 545, A101
Parisi, P., Masetti, N., Rojas, A. F., et al. 2014, A&A, 561, A67
Paturel, G., Petit, C., Prugniel, P., et al. 2003, A&A, 412, 45
Peterson, B. M. 2014, SSRv, 183, 253
Pier, E. A., & Krolik, J. H. 1992, ApJ, 401, 99
Reeves, J. N., Gofford, J., Braito, V., & Sambruna, R. 2010, ApJ, 725, 803
Ricci, C., Bauer, F. E., Arévalo, P., et al. 2016, ApJ, 820, 5
Ricci, C., Trakhtenbrot, B., Koss, M. J., et al. 2017, ApJS, in press (arXiv:1709.03989)
Ricci, C., Ueda, Y., Koss, M. J., et al. 2015, ApJL, 815, L13
Rigby, J. R., Diamond-Stanic, A. M., & Aniano, G. 2009, ApJ, 700, 1878
Robitaille, T. P., Tollerud, E. J., Greenfield, P., et al. 2013, A&A, 558, A33
Rothberg, B., & Joseph, R. D. 2006, AJ, 131, 185
Schawinski, K., Kaviraj, S., Khochfar, S., et al. 2007b, ApJS, 173, 512
Schawinski, K., Thomas, D., Sarzi, M., et al. 2007a, MNRAS, 382, 1415
Shankar, F., Bernardi, M., & Sheth, R. K. 2017, MNRAS, 466, 4029
Shen, Y. 2013, BASI, 41, 61
Shen, Y., Richards, G. T., Strauss, M. A., et al. 2011, ApJS, 194, 45
Shirazi, M., & Brinchmann, J. 2012, MNRAS, 421, 1043
Smith, K. L., Koss, M., & Mushotzky, R. F. 2014, ApJ, 794, 112
Staveley-Smith, L., Norris, R. P., Chapman, J. M., et al. 1992, MNRAS, 258, 725
Storey, P. J., & Zeippen, C. J. 2000, MNRAS, 312, 813
Tadhunter, C., Marconi, A., Axon, D., et al. 2003, MNRAS, 342, 861
Torrealba, J., Chavushyan, V., Cruz-González, I., et al. 2012, RMxAA, 48, 9
Trakhtenbrot, B., & Netzer, H. 2012, MNRAS, 427, 3081
Trakhtenbrot, B., Ricci, C., Koss, M. J., et al. 2017, MNRAS, 470, 800
Treister, E., Urry, C. M., & Virani, S. 2009, ApJ, 696, 110
Trichas, M., Green, P. J., Silverman, J. D., et al. 2012, ApJS, 200, 17
Trotter, A. S., Greenhill, L. J., Moran, J. M., et al. 1998, ApJ, 495, 740
Trump, J. R., et al. 2011, ApJ, 733, 60
Trump, J. R., Sun, M., Zeimann, G. R., et al. 2015, ApJ, 811, 26
Ueda, Y., Akiyama, M., Hasinger, G., Miyaji, T., & Watson, M. G. 2014, ApJ, 786, 104
Ueda, Y., Hashimoto, Y., Ichikawa, K., et al. 2015, ApJ, 815, 1
van den Bosch, R. C. E., Gebhardt, K., Gültekin, K., Yıldırım, A., & Walsh, J. L. 2015, ApJS, 218, 10
Vasudevan, R. V., Mushotzky, R. F., Winter, L. M., & Fabian, A. C. 2009, MNRAS, 399, 1553
Vazdekis, A., Ricciardelli, E., Cenarro, A. J., et al. 2012, MNRAS, 424, 157
Veilleux, S., & Osterbrock, D. E. 1987, ApJS, 63, 295
Veron-Cetty, M. P., & Veron, P. 2010, A&A, 518, A10
Vestergaard, M., & Peterson, B. 2006, ApJ, 641, 689
Walsh, J. L., van den Bosch, R. C. E., Barth, A. J., & Sarzi, M. 2012, ApJ, 753, 79
Wandel, A., Peterson, B. M., & Malkan, M. A. 1999, ApJ, 526, 579
Winkler, H. 1992, MNRAS, 257, 677
Winkler, H., Glass, I. S., van Wyk, F., et al. 1992, MNRAS, 257, 659
Winter, L. M., Lewis, K. T., Koss, M., et al. 2010, ApJ, 710, 503
Wold, M., Lacy, M., Käufl, H. U., & Siebenmorgen, R. 2006, A&A, 460 449
Woo, J.-H., Schulze, A., Park, D., et al. 2013, ApJ, 772, 49
Xue, Y. Q., Luo, B., Brandt, W. N., et al. 2011, ApJS, 195, 10
Yamauchi, A., Nakai, N., Sato, N., & Diamond, P. 2004, PASJ, 56, 605
York, D. G., Adelman, J., Anderson, John E., Jr., et al. 2000, AJ, 120, 1579
Yuan, F., & Narayan, R. 2004, ApJ, 612, 724